MAGNETOCALORIC EFFECT IN IRON PHOSPHIDE BASED PHASES

MAGNETOCALORIC EFFECT IN IRON PHOSPHIDE BASED PHASES

by

ALLAN HE, B. Sc. (Honours)

A thesis submitted to the School of Graduate Studies

in partial fulfillment of the requirements for the degree

MASTER OF SCIENCE

McMaster University

Hamilton, Ontario

2017

MASTER OF SCIENCE (2017)

Department of Chemistry and Chemical Biology

TITLE: Magnetocaloric Effect in Iron Phosphide Based Phases

AUTHOR: Allan He, B. Sc. (Honours) (McMaster University)

SUPERVISOR: Professor Yurij Mozharivskyj

NUMBER OF PAGES: x, 103

# Abstract

Ever since the discovery of the giant magnetocaloric effect (GMCE) in the $Gd_5(Si,Ge)_4$ phases, magnetic cooling has gained significant interest because of its potential environmental benefits and increased efficiency compared to vapour-based refrigeration. This current work is focused on one of the most promising GMCE systems, the $(Mn,Fe)_2(Si,P)$ materials. An alternative synthetic route has been explored for the $Mn_{2-x}Fe_xSi_{0.5}P_{0.5}$ and $MnFeSi_yP_{1-y}$ series which is capable of producing phase-pure samples. The new preparation technique eliminates common impurities that arise from established methods thus providing a more accurate description of the structural and physical properties. The low cost, non-toxicity, abundance of starting materials and easy tuning of the magnetic properties make these materials desirable for potential applications.

Phase-pure magnetocaloric $Mn_{2-x}Fe_xSi_{0.5}P_{0.5}$ materials (x = 0.6, 0.7, 0.8, 0.9) were synthesized through arc-melting followed by high temperature sintering. Structural features of samples with x = 0.6, 0.9 were studied through temperature dependent synchrotron powder x-ray diffraction. Magnetic measurements established the Curie temperature, thermal hysteresis, and magnetic entropy change of this system. According to the diffraction and magnetization data, all of the samples were shown to have a first-order magnetostructural transition which becomes less pronounced for Mn-richer samples.

The $MnFeSi_xP_{1-x}$ phases (x = 0.30, 0.35, 0.40, 0.48, 0.52, 0.54, 0.56) have also been synthesized by the same method. For the first time, single crystals of x = 0.30, 0.40 were successfully grown. Variable temperature x-ray diffraction experiments for x = 0.30 were completed which show the structural changes across the phase transition. This structural data was complemented with magnetization data providing Curie temperatures and thermal hysteresis.

# Acknowledgements

First off, I would like to sincerely thank my professor, Dr. Yurij Mozharivskyj who has been patient and supportive of me since day one. Thank you for providing such an ideal environment for learning, you have shown me the fun in research. I would also like to give a big thanks to my other committee member, Dr. John Greedan for satisfying my curiosity and always providing helpful advice toward my research goals.

Thank you to all the fantastic, hard-working staff of BIMR and the Department of Chemistry: the kind Dr. Hanna Dabkowska and knowledgeable Dr. Anton Dabkowski for their crystal growth expertise, Jim Garrett who never fails to put a smile on your face, Dr. Paul Dube for his help with SQUID operation and Dr. Jim Britten for all things X-ray crystallography.

Thank you to all past and present group members who have been with me the past few years. It has been such a rewarding experience because of you guys: Dr. Fang Yuan, Timothy Lo, Benson Shu Kai Ip, Dr. Mirela Dragomir, Masoud Aminzare, Dr. Scott Forbes, Dr. Zhigang Zheng, Chivarubhen Raiju Murugaanandan.

Finally, I would like to thank my family: mom and dad, my brother Lawson, for saying the right things and pushing me to be the best that I can be.

# Table of contents

# List of Figures and Tables

## Chapter 1. Symmetry

## 1.1 Symmetry Elements

In order to understand the classification of crystal structures, we must first start with the basics and introduce the different symmetry elements (**Table 1**).  In crystallography, the Hermann-Mauguin system is used to label symmetry elements and will be the notation used.  Defined generally, a symmetry element exists when the operation of the element yields no visible change in the object orientation.

**Table 1**: The list of symmetry elements that fully describe the atomic arrangement inside a crystal.

| *Element* | *Hermann-Manguin Notation* |
|---|---|
| Mirror plane | $m$ |
| Rotation axis | $n \, (2, 3, 4, 6)$ |
| Inversion center | $\bar{1}$ |
| Inversion axis | $\bar{n}$ |
| Improper rotation axis | - |
| Glide plane | $a, b, c, n, d$ |
| Screw axis | $2_1, 3_1, 4_1, 4_3, etc \dots$ |

The symmetry element of a mirror plane, represented by m, exists when for example, 2 halves of an object may be reflected across the mirror plane and take on the orientation of the opposite half.

Rotation axis, represented by n (which can take on the values of 2, 3, 4, or 6) is a rotation about the axis by 360°/n and gives an orientation of the object that looks the same as before the operation.  Note that a rotation axis may only take on the above values.  Values of n = 5 or 7 do not exist 3D periodic solid.

A center of inversion exists if the object can be reflected through the center of symmetry and an identical arrangement is found as the result.

An inversion axis is a combination of symmetry elements, namely a rotation axis and an inversion center and similar to a rotation axis, may only take on the values of $\bar{1}, \bar{2}, \bar{3}, \bar{4}, \bar{6}$. The operation of this element is the simultaneous rotation and inversion of the object.

For the sake of completeness, I have included an additional symmetry element, the improper rotation axis or alternating axis. It is rarely used in crystallography and applies more to when we are dealing with molecular symmetries, in spectroscopy. This symmetry element is another combination of symmetry elements, the rotation axis and mirror plane. It is the simultaneous operation of the two elements.

All of the discussed symmetry elements so far fall under a larger category called point symmetry because at least one point remains the same (origin) under any of the listed symmetry operations. Crystals on the other hand also possess translational symmetry. Combination of translations and rotational symmetry elements will generate new rotational symmetry elements, which are infinite.

There are a total of 5 different glide planes possible: a, b, c, n, d where n is known as the face diagonal direction and d represents the body diagonal. A glide plane is the symmetry operation of reflecting across the mirror plane followed by a

translation. The translation can be parallel to the direction of the unit cell axes (a, b, c), the face diagonal (n), or a body diagonal (d). In the cases of a, b, c, n, the translation is half of the length of the unit cell, while in the special case of a d glide plane, the translation is 1/4 of the length along the body diagonal or face diagonal.

The last one, screw axis, is another example of a space symmetry element. A screw axis is the symmetry operation of rotation, followed by a translation along the rotation axis. For example, the $2_1$ screw axis would represent a 180° rotation followed by a translation of 1/2 the unit cell edge in the direction of the rotational axis.

## 1.2 Crystal Structures

All crystals are made up of a symmetric repeating arrangement of atoms. Specifically, the *smallest* building block of the crystal from which the whole crystal can be defined is the unit cell. This may seem trivial at first, however, many choices of repeating units for a particular crystal are possible. There exists only one standardized and "correct" way of viewing it. For example, one may choose a different origin for the repeating unit while protecting all of its symmetry elements. It may also be that repeating units of different symmetry for the same crystal may also be chosen. In this case, the choice is settled by the rules below.

Rules for choosing a unit cell are listed in descending order of importance:

1) The unit cell of a crystal has the smallest volume possible.

2) The unit cell must have the highest symmetry possible.

Unit cells are classified into the following crystal systems (**Table 2**):

**Table 2**: The seven crystal systems that define the type of unit cell.

| Crystal system | Constraints | Unique symmetry element(s) |
|---|---|---|
| Cubic | $a = b = c$, $\alpha = \beta = \gamma = 90°$ | Four 3-fold rotation axes |
| Tetragonal | $a = b \neq c$, $\alpha = \beta = \gamma = 90°$ | One 4-fold rotation axis |
| Orthorhombic | $a \neq b \neq c$, $\alpha = \beta = \gamma = 90°$ | Three 2-fold rotation axes or three mirror planes |
| Hexagonal | $a = b \neq c$, $\alpha = \beta = 90°$, $\gamma = 120°$ | One 6-fold rotation axis |
| Trigonal | $a = b \neq c$, $\alpha = \beta = 90°$, $\gamma = 120°$<br>$a = b = c$, $\alpha = \beta = \gamma \neq 90°$ | One 3-fold rotation axis |
| Monoclinic | $a \neq b \neq c$, $\alpha = \gamma = 90°$, $\beta \neq 90°$ | One 2-fold rotation axis or one mirror plane |
| Triclinic | $a \neq b \neq c$, $\alpha \neq \beta \neq \gamma \neq 90°$ | - |

Every crystal structure possible can be categorized into one of these symmetries and can be further indexed as one of 230 space groups. These space groups describe the way that atoms arrange themselves in three dimensions.

Let us start with the most symmetrical building block of crystals, the cubic unit cell. A cubic unit cell can be defined by the 4 3-fold rotation axes that lie on the cube's body diagonals.

All crystal systems, except hexagonal can be obtained through distortions of the cubic unit cell. The symmetry is broken into the tetragonal unit cell when we elongate/shorten one crystallographic axis. If another axis perpendicular to the first is

altered in length, we will obtain an orthogonal cell.  From the orthogonal cell, we can obtain a monoclinic type by shear distortion of one of the faces with respect to its opposite face.  Finally, the triclinic cell (that has no symmetry) is obtained by shear distortion of a second face relative to its opposite face.

The hexagonal unit cell cannot be produced from the cubic unit cell because the layers of atoms are stacked in a different manner, which we shall see in **Chapter 1.3**.

### 1.2.1 Bravais Lattice

A crystal lattice is referred to as the whole of the periodic arrangement of atoms. It is represented by an array of discrete points which are called the lattice points.  In general, lattice points are not just atoms, they can be molecules or proteins.  The lattice point does not give any information as to what is occupying the point, only how the species are arranged.  In total, there are 5 types of centering for a lattice: P (primitive), C (base-centered), I (body-centered), F (face-centered), R (rhombohedral, only applies to hexagonal system).

In 3-dimensional space, there are 14 possible Bravais lattices (see **Figure 1**) that are obtained from the combination of the types of centering and the different crystal systems.  Other lattices that may be thought of are excluded because of symmetry requirements, or can be transformed into an existing lattice.  By convention, the base-

centering face is always perpendicular to the c axis but realistically be defined as the A or B face.

**Cubic**



F              I              P

**Tetragonal**



I              P

**Orthorhombic**



F       I       C       P

**Monoclinic**

**Triclinic**

**Hexagonal**
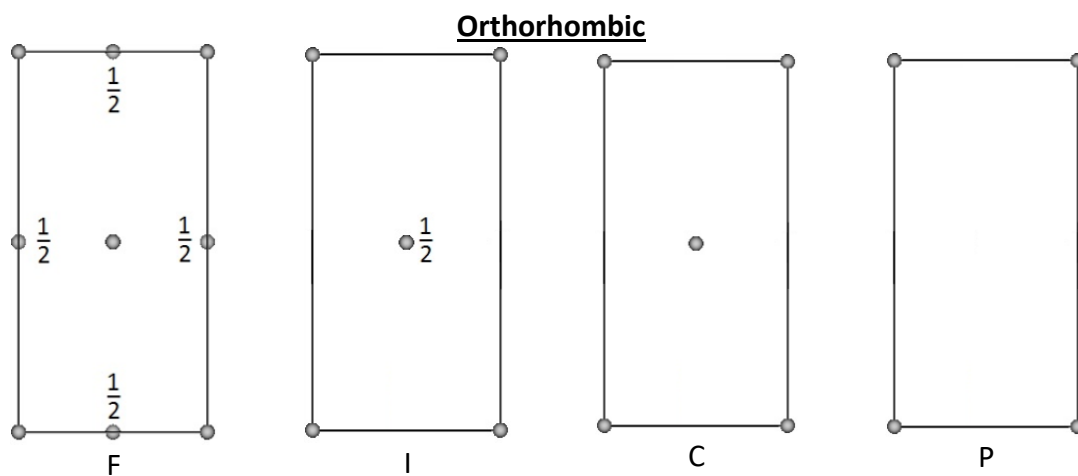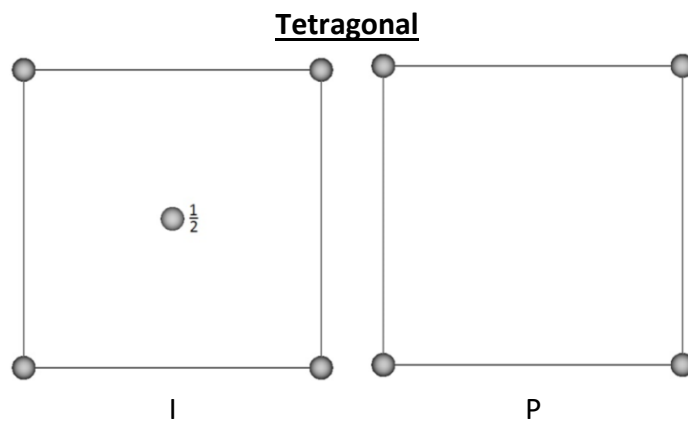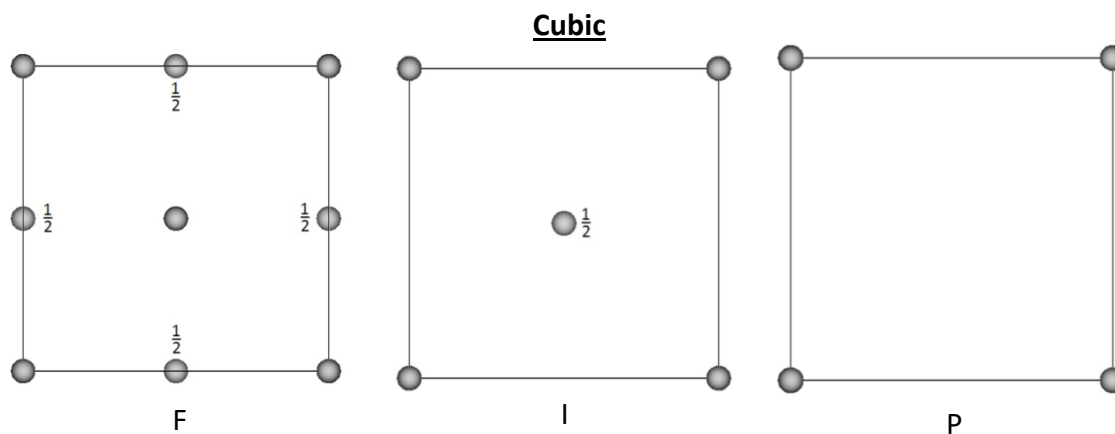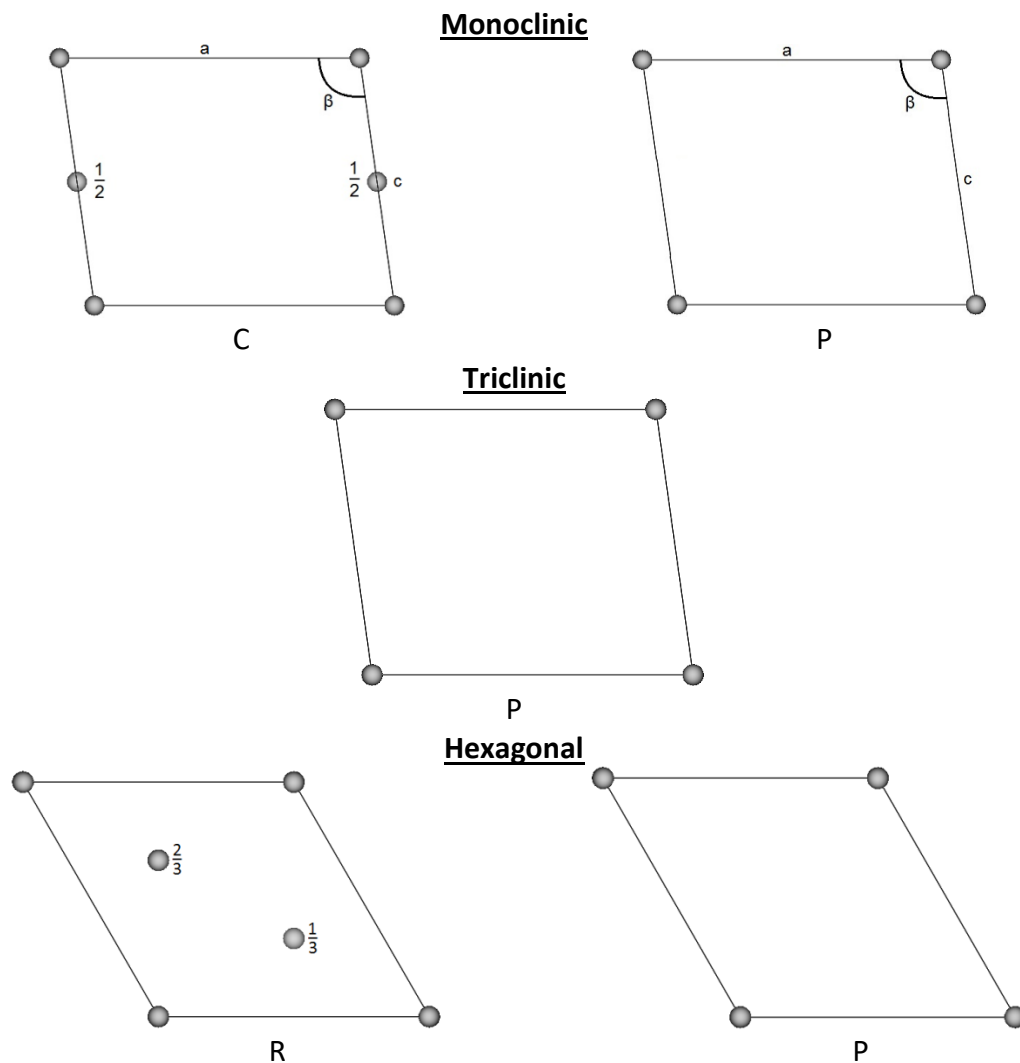
**Figure 1**: The 14 Bravais lattices arranged by crystal systems. There are a total of 5 types of centering: F (face-centered), C (C-centered), I (body-centered), R (rhombohedral), P (primitive). By convention, the monoclinic cell is usually shown with the b-axis pointing up.

### 1.2.2 Imaginary Lattice Planes

The concept of lattice planes is central to the understanding of x-ray diffraction. At its core, it is a completely imaginary construct that follows from Bragg's law (**Chapter 2.1**). Lattice planes may be assigned with 3 numbers (4 for hexagonal unit cells) known

as the Miller indices.  For example, in a cubic unit cell, the (100) plane and (110) plane are shown below in **Figure 2**:
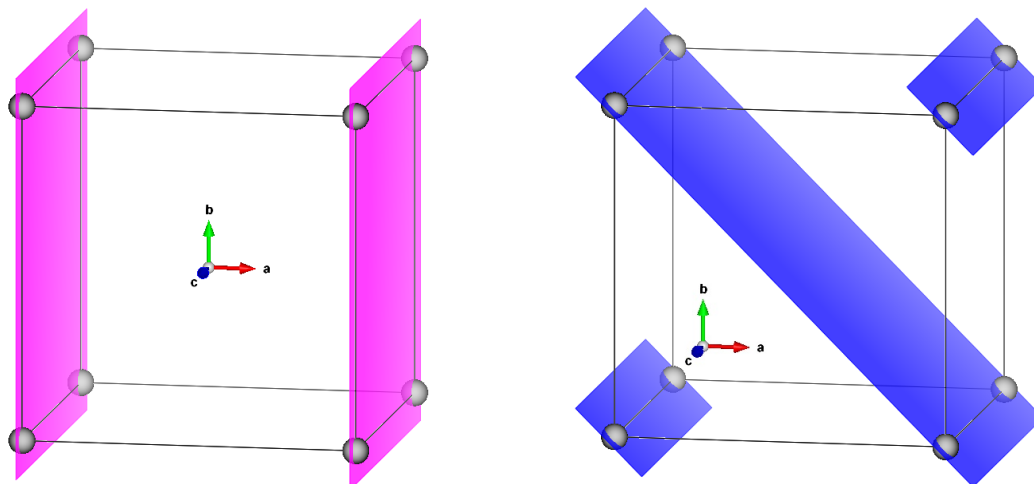


**Figure 2:** The (100) and (110) plane are indicated in magenta and blue respectively for this primitive cubic cell.

The way to assign a set of planes to its Miller indices can be done by first identifying the parallel plane beside the plane that passes through the origin.  Find the intersection of this plane with the three axes of the unit cell in terms of a, b, and c and take the reciprocal of each intercept to obtain the Miller indices.

For a particular set of planes, there is a so called d-spacing, which is the distance between adjacent planes.  A d-spacing value depends on the size and shape of the unit cell and is the d value that appears in Bragg's Law.

## 1.3 Close Packed Structures: Cubic and Hexagonal

The most efficient way to stack spheres of the same volume is to arrange them in a close

packed structure as seen below in **Figure 3**.
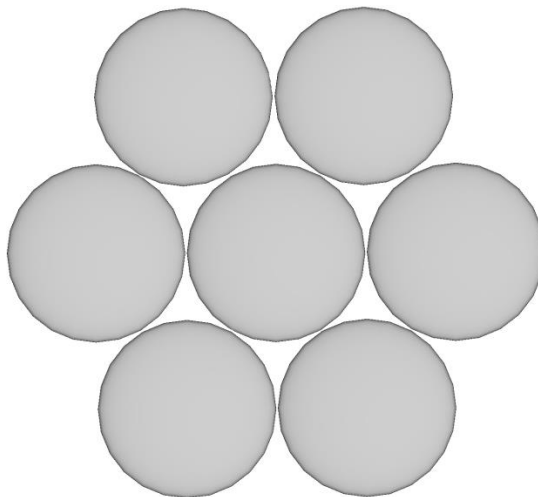
**Figure 3:** In 2-dimensions, a close packed layer is formed by arranging the circles with as little space as possible in between them without overlap.

Close packed structures can describe the atomic arrangement in many metals.

When we go to 3-dimensions, close packed layers can be stacked on each other in many

different ways, among which the hexagonal close packed structure and the cubic close

packed structure are the simplest.  Again, the idea is to minimize empty space, so the

most efficient way to pack the spheres is to put the $2^{nd}$ close packed layer in the grooves

made from the $1^{st}$ layer, not directly on top of the old spheres.  If the third layer is added

on the $2^{nd}$ layer with the same x,y coordinates as the first layer, then we obtain a

sequence ABA.   If this stacking order continues we eventually obtain: …ABABABA…

known as a hexagonal close packing.  The hcp structure is shown below in **Figure 4**:
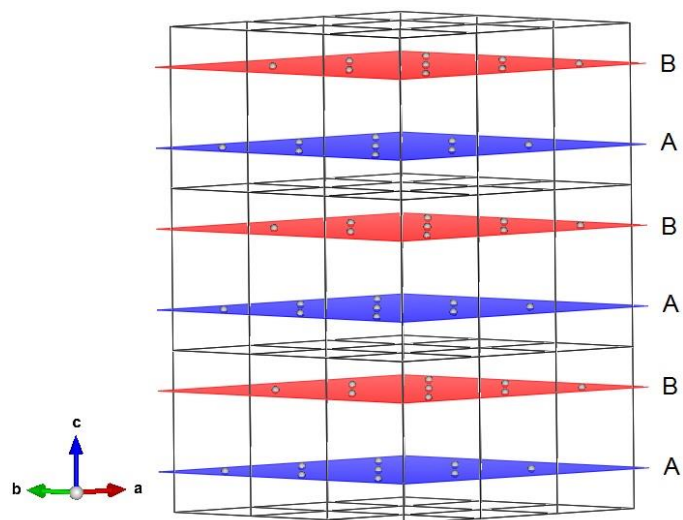
**Figure 4:** Example of hexagonal close packing.  The atoms are not shown to scale.  This simple arrangement fully describes the structure of some metals, like Zn shown here.  Other metals include Ti, Zr, Mg, etc…

It is possible to have three unique close packed layers instead of the two in hcp and obtain a new stacking order of: …ABCABC… which is known as cubic close packing. The unit cell of a ccp structure is F-centered cubic where the (111) direction is perpendicular to the close packed layers which can be seen below (**Figure 5**):
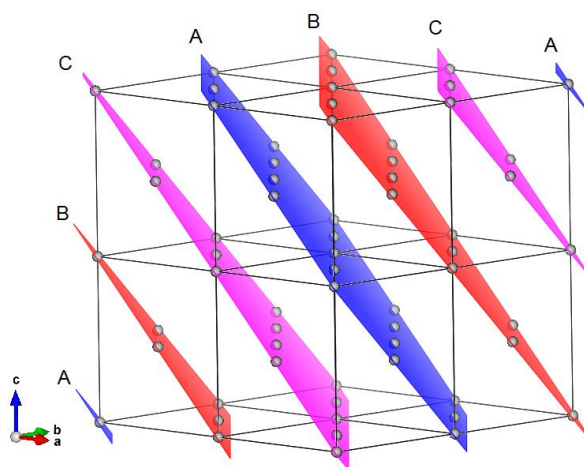


**Figure 5:** Example of cubic close packing.  Atoms are not shown to scale.  Here we have shown the structure of Cu.  Other metals that follow the ccp structure include: Ag, Au, Al, Ni, etc…

Close-packed structures have the maximum density possible assuming perfectly equal, spherical packing units. Each sphere has 12 (3 below, 6 in plane, 3 above) neighbors which is the maximum coordination number possible. Close packed structures represent only a tiny subset of the possible structure types but is a good example of the arrangement of atoms inside a solid. This basic concept can also be applied to describe the structures of alloys and ionic compounds (e.g. NaCl, ZnO, …) where the anions form a close packed layer and cations occupy the voids between the spheres.

## Chapter 2. X-ray Diffraction

Since the early 1900s, X-ray diffraction has been an extremely powerful technique capable of crystal structure determination. It is one of the main characterization techniques in solid state chemistry and a huge database of characterized solids has been compiled.

For inorganic crystalline solids, identification of the compound is routinely done by powder x-ray diffraction. In an abstract sense, the diffraction pattern of a crystal lives in reciprocal space and must be transformed back into direct space through the Fourier transform. The theory of diffraction aims to extract the crystal structure in 3-dimensional real space from reciprocal space.

We will begin our discussion with Bragg's law which is of fundamental importance to the understanding of this topic.

**2.1 Bragg's Law**

A diffraction event will only occur in the crystal when the following condition (**Eq. 1**) is satisfied:

$$2dsin\theta = n\lambda \qquad \textbf{(1)}$$

where d is the distance between the diffracted planes, $\theta$ is the angle of the incident as well as diffracted beam with regard to the planes, n is an integer. When the phase difference between the two scattered waves is a multiple of the wavelength, constructive interference occurs and a diffraction maximum is obtained. From **Figure 6**, we see that beam 2 (the beam that reflects off of plane 2) travels an extra distance, indicated by the yellow points, compared to beam 1. In order for constructive interference to occur, this distance must be equal to a multiple of the incident wavelength.
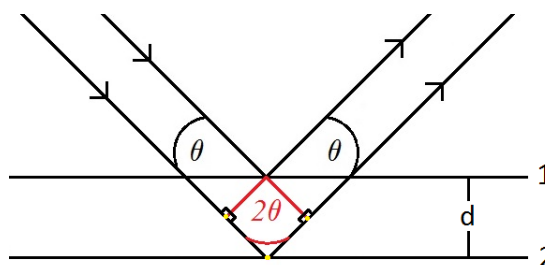


**Figure 6:** Adjacent lattice planes are indicated by 1 and 2 where d is the d-spacing. To make sure that the two beams are in phase, the extra distance traveled by beam 2 must be a multiple of the radiation wavelength.

**2.2 What are X-rays?**

X-rays is the name assigned to a region in the electromagnetic radiation spectrum that has a wavelength of ~1 Å ($10^{-10}$ m). To observe any object there needs to be a source of electromagnetic radiation and a detector. The phenomenon of diffraction can only be seen if the wavelength is the same order of magnitude as the periodic distance of the scattering objects. Visible light, as a source, does not provide the necessary resolution needed to discern the atomic arrangement inside a crystal because it is too large in wavelength. A wavelength of suitable nature to study crystal structures is that of x-rays. Typically, wavelengths between 0.5 to 2.5 Å are used since they are comparable to the shortest interatomic distances in materials.

**2.3 Generation**

There are usually two different methods to produce x-rays:

The first is using an X-ray tube. In the tube, a beam of electrons is created by heating a tungsten filament at one end. The electrons are then accelerated through a large voltage (~45000 V) and forced to hit a metal target, known as an anode (usually Cu, Co, Mo). These X-ray tubes are vacuum sealed to prevent any oxidation of the anode that may occur during the high energy collisions. This is the most commonly used method but it has some drawbacks such as usually having low efficiency and limited brightness. The spectra that results from the collisions consists of both white radiation

and multiple monochromatic wavelengths. White radiation results when electrons are slowed down or completely stopped by the metal target, converting their kinetic energy into electromagnetic radiation. When all of the kinetic energy ($\frac{1}{2}mv^2$) is converted into radiation (eV) by those electrons that are fully stopped, a lower limit to the wavelength obtained can be calculated (**Eq. 2 & 3**).

$$E = \frac{1}{2}mv^2 = eV = \frac{hc}{\lambda} \qquad \textbf{(2)}$$

Therefore, the smallest wavelength of white radiation possible is given by:

$$\lambda = \frac{hc}{eV} \qquad \textbf{(3)}$$

The monochromatic wavelengths of X-rays are the ones that are manipulated in the laboratory to do diffraction experiments, while white radiation is usually considered to be noise and is filtered out. When the electrons are accelerated toward the metal target (typically Cu or Co), some of them ionize the Cu 1s electrons. The vacancy is quickly occupied by an outer orbital electron (2p or 3p) and the energy released as a result of the transition has a characteristic wavelength. Names are given depending on whether it is the 2p -> 1s transition (Kα) or 3p -> 1s (Kβ) transition which have wavelengths of approximately 1.5418 Å and 1.3922 Å respectively, for Cu radiation. Generally, Kα radiation is used because the transition occurs more frequently and is therefore more intense than Kβ. The total angular momentum (j) of the electron prior to the transition would be slightly different depending on which of the two possible spin

states (up or down) is adopted, and so the energy required for the transition would also be different. This results in the $K\alpha$ radiation being a doublet ($K\alpha_1$, $K\alpha_2$) in the x-ray spectra, rather than a single peak.

The second x-ray source is the synchrotron, a much more advanced technique. They are the most powerful x-ray radiation sources available today. Electromagnetic radiation is produced by accelerating electrons to relativistic velocities. They are guided by bending magnets and circulate in ultra-high vacuum tubes. The x-rays that are produced from this process are incredibly intense leading to very high resolution powder patterns. The wavelength of radiation can also be tuned very precisely allowing for experiments such as XANES (X-ray Absorption Near-Edge Spectroscopy) which reveals information about the local symmetry of the element.

## 2.4 Collimation

The raw x-ray beam contains high background noise due to the presence of white radiation as well as several strong, characteristic peaks due to the $K\alpha_1$, $K\alpha_2$, $K\beta$ transitions. In addition to this, the angular divergence of the raw beam would make Bragg peaks look broad and asymmetric and so some kind of filtering and collimation must be established.

Collimation of the beam is done primarily through using a divergence slit and soller slit. The divergence slit determines how much of the beam is allowed in the plane

of the goniometer axis while the soller slit determines the angular divergence in the orthogonal direction.

One of the simplest ways to get clean data that can be easily analyzed is to introduce a filter for the incoming x-ray beam to help get a monochromatic light source. The general rule in choosing a filter is to pick a material with one atomic number less than the anode material. For example, if we are dealing with a Cu anode source then Ni would be a suitable filter. This ensures that the absorption edge is in between the $K\alpha_1$ and $K\beta$ lines so that everything below the absorption edge is drastically lowered in intensity and we are left with only $K\alpha_1$ and $K\alpha_2$ peaks. Such a material is called a β filter.

More sophisticated methods of monochromatization can be achieved by using single crystals. If the single crystal is placed at the correct position, the incoming wavevector of raw x-rays can be diffracted only at a specific angle according to Bragg's law. The selected wavelength will be the only one that reaches the sample which substantially increases the resolution of a powder diffraction pattern.

## 2.5 Reciprocal Lattice and Ewald's Sphere

To simplify the discussion of diffraction, the ideas concerning reciprocal space are introduced. The concept of Ewald's sphere and the reciprocal lattice are entirely imaginary constructs and should be treated as tools in understanding diffraction.

Let $\boldsymbol{a}$, $\boldsymbol{b}$, and $\boldsymbol{c}$ represent the translations of a three-dimensional lattice in real space. The reciprocal lattice can then be defined by three other translations, $\boldsymbol{a}^*$, $\boldsymbol{b}^*$, and $\boldsymbol{c}^*$ (**Eq. 4**):

$$\boldsymbol{a}^* = \frac{\boldsymbol{b} \times \boldsymbol{c}}{V} \qquad \boldsymbol{b}^* = \frac{\boldsymbol{c} \times \boldsymbol{a}}{V} \qquad \boldsymbol{c}^* = \frac{\boldsymbol{a} \times \boldsymbol{b}}{V} \qquad (4)$$

where $\times$ represents the cross product, and V is the volume of the unit cell in direct space.

The length of reciprocal lattice vector ($\boldsymbol{d}^*$) (**Eq. 5**) is inversely proportional to the interplanar distance, $d$, and is perpendicular to the corresponding crystallographic plane.

$$|\boldsymbol{d}^*| = \frac{1}{d} \qquad (5)$$

Consider an incident x-ray beam with wavelength $\lambda$ and with wavevector $k_0$ (**Eq. 6**):

$$k_0 = \frac{1}{\lambda} \qquad (6)$$

The scattered wave will be represented by $k_1$ and is equal to $k_0$. Assuming that the head of $k_0$ corresponds with the origin of the lattice, a diffraction event in the $k_1$ direction will only happen when its head touches a reciprocal lattice point (see **Figure 7**). Since the length of both vectors is the same, and the $k_0$ direction is fixed to the origin, all possible orientations of $k_1$ will produce Ewald's sphere. Whenever this sphere

intersects with a reciprocal lattice point, then a diffraction event will occur. This model is incredibly powerful in the understanding of x-ray diffraction.

It is worth mentioning that in reality, due to the slight deviation of wavelength in the monochromatized beam and crystal defects, Ewald's sphere has a finite thickness and the reciprocal lattice points are much larger than mere points. This gives some amount of leeway for a diffraction event to occur at a specific $2\theta$, which is the angle between $k_0$ and $k_1$ in this model.
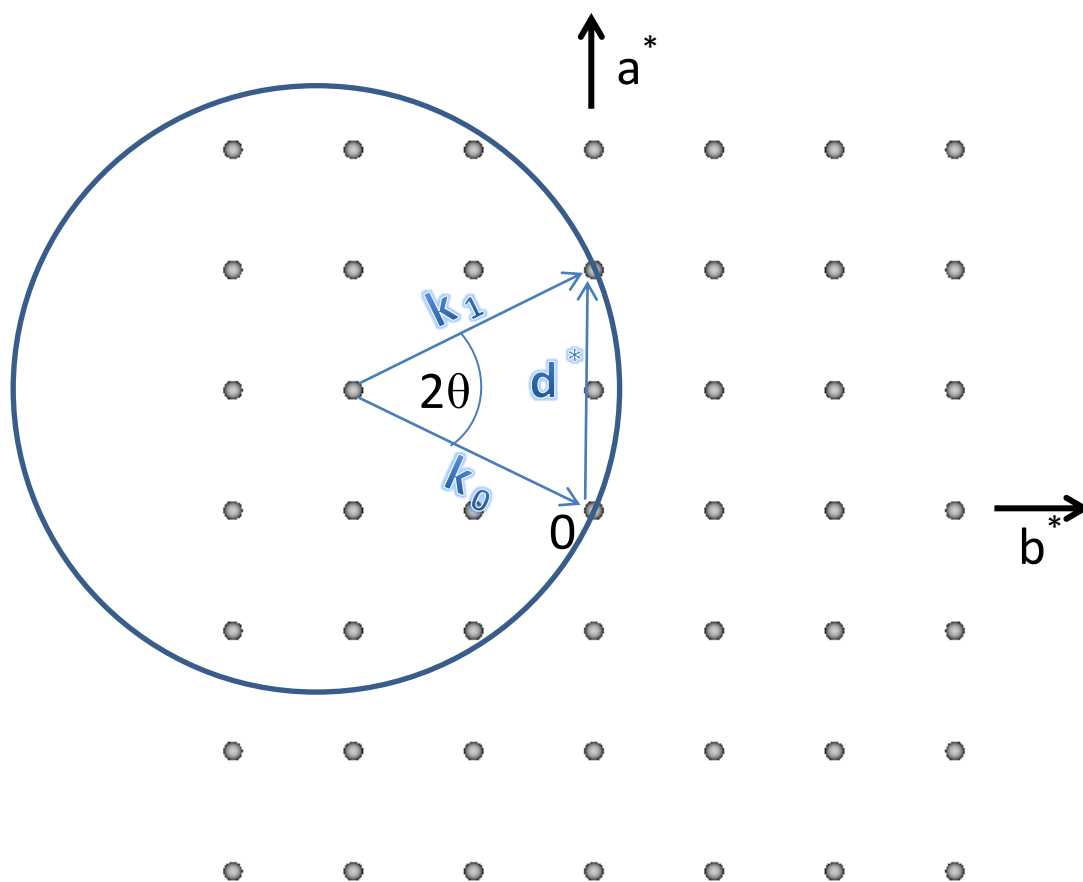


**Figure 7:** A 2-dimensional version of Ewald's sphere. A diffraction event will occur when the surface of the sphere touches any reciprocal lattice point other than the origin.

## 2.6 Structure Factor $(|F_{hkl}|^2)$

The structure factor (**Eq. 7**) is arguably the most important parameter for structure solutions. It is defined as the square of the absolute value of structure amplitude $(|F_{hkl}|)$ and is directly proportional to the intensity of the diffracted beam. It is made up of many important parameters which will be discussed in detail. The structure amplitude is written as:

$$F_{hkl} = \sum_{j=1}^{n} g_j t_j \left(\frac{\sin\theta_{hkl}}{\lambda}\right) f_j \left(\frac{\sin\theta_{hkl}}{\lambda}\right) e^{2\pi i(hx_j + ky_j + lz_j)} \tag{7}$$

where $j$ is an atom counter, $n$ is the total number of atoms in the unit cell, $g$ is the population factor, $t$ is the displacement parameter, $f$ is the specific atomic scattering factor.

## 2.6.1 Population factor $(g)$

The population factor accounts for the atom occupancy in the unit cell and takes on the values between 0 (completely absent) and 1 (fully occupied). Not all of the sites may be occupied in the unit cell, some atoms may be missing due to defects, or may lie close to a symmetry element which will have a $g$ that is smaller than 1.

Often, the distance between this atom and its symmetrical partner are unrealistically too close. In this case, the population of the atom in the site will be dependent on the multiplicity of the symmetry element. For example, the multiplicity of

a mirror plane would be 2, and therefore the population of the two atoms would be $\frac{1}{2}$. The atom would be found on the one side of the plane half of the time and on the other side, the other half of the time.

### 2.6.2 Displacement Parameter ($t$)

The displacement factor primarily deals with describing the vibrations of the atoms which is made up of several different effects. The displacement of the atom from its equilibrium position is oscillatory in nature and is their movement is defined by the phonon modes that can be excited at the temperature of the material. Other effects that are also at play include chemical bonding and how it changes the electron density around the atom, anisotropy of the sample, and absorption. In the isotropic approximation, the temperature factor takes on the form seen in **Eq. 8**:

$$t_j = e^{-B_j\left(\frac{\sin\theta}{\lambda}\right)^2} \tag{8}$$

where $B_j = 8\pi^2(\bar{u}_j{}^2)$ is the parameter for the atomic displacement in terms of $\bar{u}$ (root mean square deviation from equilibrium position). Typical values of $B_j$ are around $0.5 - 1$ Å$^2$ for intermetallics while for organic and organometallic compounds, the range may be as large as $3 - 10$ Å$^2$.[2]

### 2.6.3 Atomic Scattering factor ($f$)

Atoms are capable of diffracting or scattering an incoming x-ray beam because of its interaction with the electrons. Recall that electrons are charged particles that are influenced by the oscillating electric field and magnetic field of the x-ray radiation. The oscillatory electric field and magnetic field of light make the electrons vibrate. When x-rays come into contact with a sample, three different processes may occur:

1) Coherent scattering: energy of the photons after being coherently scattered remain the same compared to the incident beam. If the radiation is scattered elastically, then no energy loss happens and the wavelength will stay the same. During this process, the electron will accelerate and decelerate due to the imposed field and release radiation of the same frequency as the incident wave

2) Incoherent scattering: energy of the photons in the scattered beam decreases due to collisions with core electrons (Compton effect).

3) Absorption: photons scatter in random directions and can lose their energy by kicking out electrons from an atom resulting in ionization through the photoelectric effect.

Only coherent, elastic scattering will be considered in the following discussion. The intensity of the scattered beam depends on the phase difference between the incident beam and scattered beam (see **Figure 8**). Fully constructive interference leads

to the maximum intensity possible while complete destructive interference would result in 0 intensity.

Consider the following diagram:
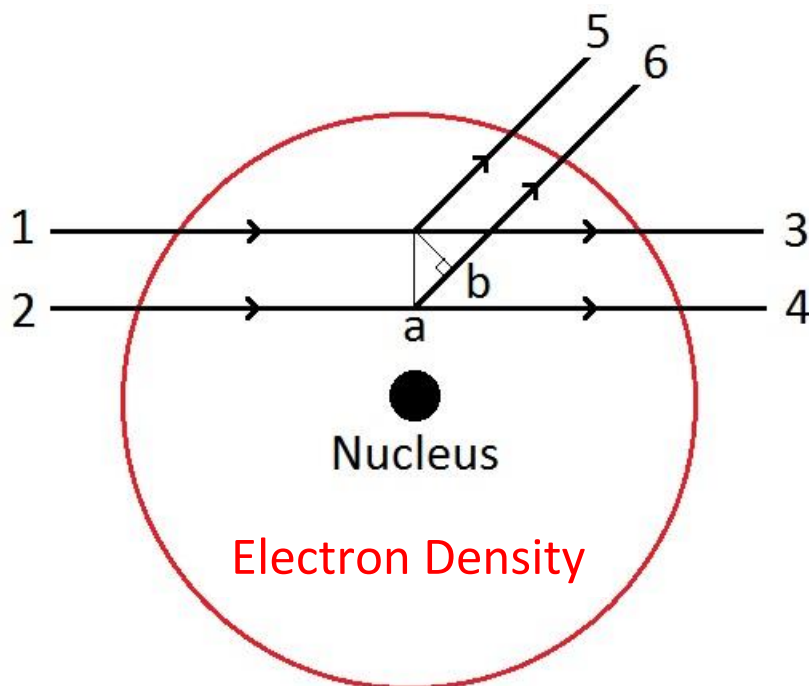


**Figure 8:** Illustrating the phase difference induced by scattering from electrons at different parts of the atom. We are assuming a completely spherical distribution of electrons.

For simplicity, we will just consider two beams of incident x-rays, 1 and 2. In reality, the x-ray beam travels as a plane wave and is made up of a large amount of beams. The beam paths, 13 and 24 are completely unaltered and there will be no phase difference between the incident and scattered beam. In the case that the beam is scattered at a finite angle (paths 15 and 26), we see that the path of 26 is elongated by the distance, ab, compared to the path 15. This phase difference results in destructive interference (the distance ab is usually much smaller than the wavelength of radiation

since the distance between electrons of the same atom is very small) that makes the observed scattered intensity lower.  The larger the angle, the smaller intensity observed for the scattered beam.  One of the consequences of this is very weak intensities at high angles in XRD patterns.

For each specific atom, there exists a characteristic atomic form factor (or atomic scattering factor) given by **Eq. 9**:

$$f_j \left( \frac{\sin \theta}{\lambda} \right) = c_0 + \sum_{i=1}^{4} a_i e^{-b_i \frac{\sin \theta}{\lambda}} \tag{9}$$

where $c_0$, $a_i$, $b_i$ are coefficients that are specific to the j$^{th}$ atom.

The intensity of scattered beam also increases with atomic number.  Because of this, light atoms cannot be characterized very well, and it is hard to distinguish between adjacent elements in the periodic table using x-ray diffraction.

**2.7 Fourier Transform**

Real space and reciprocal space are related by the Fourier transform (see **Eq. 10 & 11**).  It serves the purpose of decomposing a function into sinusoidal components.  Any function may be written as the sum of sinusoidal functions.  The electron density ($\rho$) in real space may be transformed into scattering amplitude ($\Phi$) in reciprocal space.

$$\Phi_{hkl} = \int_V \rho_{xyz} e^{2\pi i(hx+ky+lz)} d^3x \qquad \textbf{(10)}$$

$$\rho_{xyz} = \int_{V^*} \Phi_{hkl} e^{-2\pi i(hx+ky+lz)} d^3h \qquad \textbf{(11)}$$

Since the electron density is periodic in nature for a crystal, we can rewrite the integral as **Eq. 12**:

$$\rho(x) = \frac{1}{V} \sum_{h=-\infty}^{h=\infty} \sum_{k=-\infty}^{k=\infty} \sum_{l=-\infty}^{l=\infty} F_{hkl} e^{-2\pi i(hx+ky+lz)} \qquad \textbf{(12)}$$

where $F$ is a complex number and are the structure amplitudes.

In a diffraction experiment, only absolute values of the structure amplitude are obtained and so **Eq. 12** can be rewritten into **Eq. 13**:

$$\rho(x) = \frac{1}{V} \sum_{h=-\infty}^{h=\infty} \sum_{k=-\infty}^{k=\infty} \sum_{l=-\infty}^{l=\infty} |F_{hkl}| \cos(2\pi(hx + ky + lz) - \alpha_{hkl}) \qquad \textbf{(13)}$$

where $\alpha$ is the phase angle for the specific reflection. For centrosymmetric (contains inversion center) structures, $\alpha$ is equal to $0, \pi$ while for non-centrosymmetric structures, the phase angle must be calculated.

## 2.8 Powder X-ray Diffraction

For polycrystalline samples, powder x-ray diffraction is the main technique used for characterization. The sample that we are interested in analyzing is crushed into a

fine powder. It is important to emphasize that the sample should be crushed finely enough and spread evenly so that ideally the sample has crystallites randomly oriented in all directions. Toluene containing a small amount of Vaseline is spread across the top of a silicon wafer. Once the solvent has evaporated, a thin layer of Vaseline remains on the surface and the powder is dispersed evenly on the top of the wafer. The silicon wafer is a single crystal of silicon that has been cut and polished along a specific direction to produce no diffraction peaks in the background. This acts as an ideal sample holder.

Once the incoming x-ray beam has been monochromatized and strikes the sample, the diffracted beam in fact takes on the shape of a cone, due to the crystallites being present at all orientations (see **Figure 9**). A specific set of planes will emit its own cone of radiation with an angle $\theta$ that satisfies Bragg's Law. The cone shape is produced because there are no restrictions on the angular orientation of the planes with respect to the incident beam. Since the powder sample has crystallites in every direction, the diffracted beams of all the crystallites give the appearance of a cone.
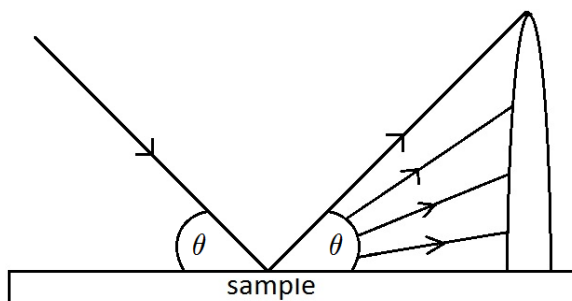


**Figure 9:** Diffracted cone of radiation in a powder x-ray diffraction experiment.

The powder method is capable of identifying the crystalline phase but gives no direct data about the composition of the sample. Each phase has its own unique d-spacing and intensity that are outcomes of the specific atomic arrangement. The d-spacing depends on the symmetry of the unit cell and lattice parameters. The intensity depends on many parameters which were previously discussed in **Chapter 2.6** to **Chapter 2.6.3**.

A general rule is that crystals with higher symmetry will have fewer peaks produced in the powder pattern compared with low symmetry unit cells. We may illustrate this by comparing a cubic unit cell with an orthorhombic unit cell. In a cubic unit cell, a reflection (h00) would have a multiplicity of 6 since indices of (h00, -h00, 0k0, 0-k0, 00l, 00-l) are all the same. All of these reflections have the same d-spacing and will appear at the same angle. In the orthorhombic unit cell, the same reflection (h00) has a multiplicity of 2 since only (h00) and (-h00) have the same d-spacing. The other reflections would appear as 2 separate peaks: (0-k0) and (0k0), (00l) and (00-l).

## 2.9 Rietveld Refinement

The foundation of the Rietveld method and refining powder x-ray diffraction patterns lies on minimizing the difference between the experimental data and a calculated powder diffraction profile.

Assuming high quality powder diffraction data, the success of Rietveld refinement hinges on the experience of the user to properly select a sequence in which the parameters are refined. These variables include the peak shape parameters, unit cell dimensions, background, scale factor, fractional coordinates, atomic displacement factor, to name a few. A least-squares approach is applied during Rietveld refinement to converge to the final values of the parameters. The Rietveld method is solely a refinement technique, and it requires, a priori, a model of the crystal structure.

### 2.9.1 Non-linear Least Squares Minimization

The function in which we are interested in minimizing is $\Phi$, given in **Eq. 14**:

$$\Phi = \sum_{i=1}^{n} w_i \left( Y_i^{obs} - Y_i^{calc} \right)^2 \tag{14}$$

where $w_i$ is the weight factor for the $i^{\text{th}}$ data point, $Y_i^{obs}$ is the observed intensity and $Y_i^{calc}$ is the calculated intensity of point $i$, $n$ is the total number of points.

In the case of monochromatic radiation and assuming a single phase composition, the calculated intensity can be expanded into **Eq. 15**:

$$\Phi = \sum_{i=1}^{n} w_i \left( Y_i^{obs} - (b_i + K \sum_{j=1}^{m} I_j y_j(x_j)) \right)^2 \tag{15}$$

where $b_i$ is the background value for point $i$, $K$ is the scale factor for the single phase, $m$ indicates the number of Bragg reflections that contribute to the intensity at $i$ (since

multiple peaks may overlap), $I_j$ represents the integrated intensity for the $j^{\text{th}}$ Bragg reflection, and $y_j$ is the peak shape function dependent on $x_j = 2\theta_j^{calc} - 2\theta_i$.

This equation stresses the importance of a low background value. In the case of a small background (namely when $b_i$ is much smaller than $K\sum_{j=1}^{m} I_j y_j(x_j)$), then the function is minimized based on the peak shape parameters and the integrated intensities like it is supposed to. On the other hand, if the background is very large ($b_i \geq K\sum_{j=1}^{m} I_j y_j(x_j)$) then the least squares refinement will be based largely on the background value and not on the shape of the peaks.

In the case of a sample that has multiple phases, we can add a summation sign which ranges until the final p phase (see **Eq. 16**).

$$\Phi = \sum_{i=1}^{n} w_i \left( Y_i^{obs} - (b_i + \sum_{z=1}^{p} K \sum_{j=1}^{m} I_j y_j(x_j)) \right)^2 \tag{16}$$

**2.9.2 Quality of Refinement**

To judge the quality of refinement, we may refer to the difference plot between the measured and calculated intensities. For an ideal refinement, the difference spectrum should be 0. It is also common to refer to certain figures of merit: the profile residual or reliability factor ($R_p$, **Eq. 17**), the weighted profile residual ($R_{wp}$, **Eq. 18**), the expected profile residual ($R_{exp}$, **Eq. 19**), and goodness of fit ($\chi^2$, **Eq. 20**).

$$R_p = \frac{\sum_{i=1}^{n}\left|Y_i^{obs} - Y_i^{calc}\right|}{\sum_{i=1}^{n}\left|Y_i^{obs}\right|} \times 100\% \tag{17}$$

$$R_{wp} = \sqrt{\frac{\sum_{i=1}^{n} w_i\left(Y_i^{obs} - Y_i^{calc}\right)^2}{\sum_{i=1}^{n} w_i\left(Y_i^{obs}\right)^2}} \times 100\% \tag{18}$$

$$R_{exp} = \sqrt{\frac{n-p}{\sum_{i=1}^{n} w_i\left(Y_i^{obs}\right)^2}} \times 100\% \tag{19}$$

$$\chi^2 = \left(\frac{R_{wp}}{R_{exp}}\right)^2 \tag{20}$$

where n is the total number of data points, p is the number of free least squares parameters.

**Chapter 3. Magnetism**

**3.1 Orbital Angular Momentum and Spin**

There exist two contributions to the magnetic moment of a free atom. The first is due to the orbital motion of the electron around the nucleus which generates orbital angular momentum. The second comes from the fact that each electron possesses an intrinsic magnetic moment due to its "spin". With the addition of an external field, an extra contribution arises from the change in orbital angular momentum due to the applied field. We shall start off our discussion of magnetism by showing the quantization of orbital angular momentum and spin.

Let us assume that an external magnetic field is applied along the z-axis. In the solution of Schrodinger's equation for the hydrogen atom, it is observed that the quantum numbers $l$ and $m_l$ could only take on certain values. The magnitude of the orbital angular momentum is given by **Eq. 21**:

$$|L| = \sqrt{l(l+1)}\hbar \tag{21}$$

The magnitude of the magnetic moment that comes from the orbital angular momentum is $g_L\sqrt{l(l+1)}\mu_B$ ($g_L = 1$) and the component of the magnetic moment along the z-axis is $-g_L m_l \mu_B$.

The second contribution to the magnetic moment, the electron spin is not predicted in the solution of Schrodinger's equation because it is the result of relativistic effects which were not considered. Associated with the electron spin are the quantum numbers, $s$ and $m_s$. Quantum number $s$, always takes on a value of 1/2 for electrons. The z-component of the spin is quantized ($m_s$) and can only assume a total of $2s+1$ discrete values (called its multiplicity), namely, {-s, -s+1, ..., s} which turn out to be -1/2 and 1/2. Therefore, the component of spin angular momentum along the field direction is then $\pm\hbar/2$ and a magnitude equal to that seen in **Eq. 22**:

$$|S| = \sqrt{s(s+1)}\hbar = \frac{\sqrt{3}}{2}\hbar \tag{22}$$

The magnitude of the magnetic moment that comes from the spin angular momentum is $g_S\sqrt{s(s+1)}\mu_B$ ($g_S \approx 2$). When the spin angular momentum is

associated with a magnetic moment, it will have a component along the z-axis equal to

$-g_S m_s \boldsymbol{\mu_B}$.

The energy of the electron (**Eq. 23**) in a magnetic field is then:

$$E = \mu_0 g \mu_B m_s H \tag{23}$$

We can see from this equation that the energy levels are split by the magnetic

field by the amount: $\mu_0 g \mu_B H$, called the Zeeman splitting.

## 3.2 Spin-orbit Coupling

As seen above, magnetic moments arise in the electron from the orbital motion

of the electron around the nucleus, as well as from its inherent spin. The interaction

between the magnetic moment of the electron's spin with the magnetic field originating

from its orbital motion is called spin-orbit coupling.

In general, $\boldsymbol{L}$ and $\boldsymbol{S}$ are not separately conserved because of this coupling

however, the total angular momentum $\boldsymbol{J} = \boldsymbol{L} + \boldsymbol{S}$ is. The way to calculate total angular

momentum $\boldsymbol{J}$ depends on the relative strength of spin-orbit, orbit-orbit, and spin-spin

coupling. Different coupling regimes are presented in the next two sections (**Chapter

3.2.1 and Chapter 3.2.2**).

### 3.2.1 Russell-Saunders (L-S) Coupling

In the case of light atoms, the orbit-orbit and spin-spin couplings will be the dominant energy terms rather than the spin-orbit coupling due to low Z. We must then consider combining separately the orbital angular momenta and spin angular momenta first prior to bringing in the spin-orbit interaction.

For simplicity, we can study the example of an atom with just two electrons. The electrons would have orbital angular momentum quantum numbers $l_1$ and $l_2$ and spin quantum numbers $s_1$ and $s_2$ respectively.

The allowed values of $L$ and S are then given by **Eq. 24** and **25**:

$$L = l_1 + l_2, l_1 + l_2 - 1, \ldots, |l_1 - l_2| \tag{24}$$

$$S = s_1 + s_2, s_1 - s_2 \tag{25}$$

Therefore for the whole atom, we must define $M_L \in \{-L, -L+1, \ldots, L\}$ and $M_S \in \{-S, -S+1, \ldots, S\}$.

The total angular momentum quantum number, $J$, is then determined by addition of the total atomic orbital angular momenta and spin (**Eq. 26**):

$$J = L + S, L + S - 1, \ldots, |L - S| \tag{26}$$

Similarly, we define $M_J \in \{-(L+S), -(L+S)+1, \ldots, L+S\}$. The magnitude of the total atomic angular momentum, $|J|$ is shown below (**Eq. 27**):

$$|\boldsymbol{J}| = \sqrt{J(J+1)}\hbar \qquad \textbf{(27)}$$

We may calculate the magnetic moment using $\boldsymbol{J}$, in similar fashion to the $\boldsymbol{L}$ and $\boldsymbol{S}$ equations seen above which is equal to $g_J\sqrt{J(J+1)}\boldsymbol{\mu_B}$ where $g_J$ (**Eq. 28**) is equal to:

$$g_J = \frac{3}{2} + \frac{S(S+1) - L(L+1)}{2J(J+1)} \qquad \textbf{(28)}$$

under the assumption that $g_S = 2$ and $g_L = 1$.

### 3.2.2 j-j Coupling

In the case of heavy atoms like the actinides, a different coupling method must be used since the spin-orbit interaction becomes the dominant energy term. The orbital angular momenta and spin angular momenta combine first (shown in **Eq. 29**) to give the total angular momentum for a specific electron, n:

$$j_n = l_n + s_n \qquad \textbf{(29)}$$

The j's obtained are then summed (**Eq. 30**) to get the total angular momentum of the atom:

$$J = \sum_n j_n \qquad \textbf{(30)}$$

**3.3 Hund's Rules**

The ground state configuration of electrons in an incomplete shell of an atom can be estimated using three rules. These rules are listed in order of importance. In other words, rule 1 must be satisfied before rule 2, and so on.

1) Maximize S. This rule deals with spin-spin interaction. The lowest energy state will be given for a term with the highest multiplicity (2S+1). Physically, this means that the electrons prefer to keep their spins parallel and be put in orbitals one at a time until each orbital has only a single electron. By singly occupying the different spatial orbitals, the unpaired electrons experience decreased shielding from the nucleus compared to a doubly occupied orbital. The Coulomb energy is kept to a minimum in this way by reducing repulsion that would occur if an electron were to occupy an orbital with an electron already there.

2) Maximize L. This rule deals with orbit-orbit interaction. Electrons must occupy an orbital with greatest orbital angular momentum. Due to the restrictions set by the first rule, electrons must singly occupy all the orbitals available. The second rule then states that electrons will start to pair up in the ones with greatest L. This can be understood using classical arguments. Angular momentum is given by **Eq. 31**:

$$L = mvr \tag{31}$$

Since m and v stay the same for an electron, the radius of the orbit is larger with bigger L. Therefore, if two electrons occupy an orbital with a bigger radius, they are less likely to meet each other than if they were to occupy a smaller orbital. Coulomb repulsion is minimized.

3) Maximize J if shell is more than half full ($J = |L + S|$). Minimize J if less than half full ($J = |L - S|$). This rule deals with minimizing the spin-orbit interaction. As we have seen above, the spin-orbit coupling is only significant in heavy atoms. In light atoms such as the 3d elements, the spin-orbit energies are not as significant as, for example, the crystal field energy term making the $L$ almost irrelevant and often "quenched".

**3.4 Crystal Field Interactions and Quenching of Orbital Angular Momentum**

In the case of 3d metal ions, the expected ground states do not match the ones predicted by experiment. The predicted moment of $\mu_B g_J \sqrt{J(J+1)}$ do not agree with experiment (however, it does work well for the heavy transition metals and lanthanides) and in fact more closely matches $\mu_B g_S \sqrt{S(S+1)}$. This phenomenon has been called orbital quenching the data is consistent with the case when $J = S$ and $L = 0$. This effect has its origin from the crystal field interactions around the ion which turns out to be stronger than the spin-orbit coupling term. The crystal field splitting is the result of electrostatic interactions among the ions which breaks the spherical symmetry of a free atom, and forces the symmetry of the crystal onto the electron density.

Hund's third rule assumes that the spin-orbit coupling term is the next most significant to Coulombic effects which turns out not to be true in the case of light 3d metal ions. In the heavier 4d and 5d metal ions, the case becomes less clear since the two effects start to become comparable.

### 3.5 Magnetic Field ($H$)

We may start our discussion by defining what a magnetic field ($H$) is. It is an experimental fact that the force between two magnetic poles is directly related to how strong they are, and how far apart they are. This may be stated mathematically by **Eq. 32**:

$$F = \frac{\mu_0}{4\pi}\frac{p_1 p_2}{r^2} = \mu_0 H p_2 \qquad \text{(32)}$$

where $\mu_0 = 4\pi \times 10^{-7}\ N/A^2$ is the permeability of free space, and the strength of the poles is measured in $A \cdot m$. The magnetic field can be defined as the force generated by $p_1$ exerted on $p_2$.

### 3.6 Magnetization ($M$) and Magnetic Induction ($B$)

From experiment it is known that all materials will gain some magnetic moment ($m$) when placed into a magnetic field ($H$). The magnetization ($M$) is defined as the dipole moment per unit volume (**Eq. 33**):

$$M = \frac{m}{V} \tag{33}$$

The response of a material to an applied field is called the magnetic induction (**B**) and is given by **Eq. 34**:

$$\boldsymbol{B} = \mu_0(\mathbf{H} + \mathbf{M}) \tag{34}$$

In free space however, there is no magnetization so the magnetic induction becomes linearly related to the magnetic field (**Eq. 35**):

$$\boldsymbol{B} = \mu_0\mathbf{H} \tag{35}$$

### 3.7 Magnetic Moment ($m$) and Bohr Magneton ($\mu_B$)

The magnetic moment of an atom can be defined as **Eq. 36**:

$$\boldsymbol{m} = I \int d\boldsymbol{S} \tag{36}$$

where $d\boldsymbol{S}$ is the area of the loop that the electron is traveling in. As the electron orbits the nucleus, a current $I = -\frac{e}{\tau}$ (**Eq. 37**) is generated where $\tau = \frac{2\pi r}{v}$ is the orbital period, v is the speed and r is radius of orbit.

$$I = -\frac{e}{\tau} = -\frac{ev}{2\pi r} \tag{37}$$

The angular momentum of the electron in the ground state is: $L = m_e v r = \hbar$. Substituting everything back into the magnetic moment formula (**Eq. 36**), we obtain **Eq. 38**:

$$\boldsymbol{m} = I\pi r^2 = -\frac{ev}{2\pi r}(\pi r^2) = -\frac{evr}{2} = \frac{e\hbar}{2m_e} = -\boldsymbol{\mu_B} \tag{38}$$

The magnetic moment of an electron is usually expressed in units of $\boldsymbol{\mu_B}$.

## 3.8 Exchange Interaction (Two-Electron System)

Now that we know the origin of the magnetic moment and how it behaves as a free atom, we can start to discuss about how magnetic moments interact with each other. The exchange interaction is the basis for long range magnetic order. This interaction lies at the heart of ferromagnetism, has no classical analogue, and originates from the overlap of electronic wave functions.

### 3.8.1 Spatial and Spin Functions

For simplicity we shall only consider a model which consists of just two electrons that have spatial wavefunctions $\psi_a(r_1)$ and $\psi_b(r_2)$. The joint state of these electrons can be written as the product, $\psi_a(r_1)\psi_b(r_2)$. From the Pauli exclusion principle, we know that the overall wavefunction must be antisymmetric with respect to the exchange of two electrons. Currently, if we were to exchange the two electrons, we would get $\psi_a(r_2)\psi_b(r_1)$ which would not satisfy the principle because it is not a multiple of the original product. The principle would be satisfied by taking the linear combination of the two and normalizing (**Eq. 39**):

$$\Psi_{spatial}(r_1, r_2) = \frac{\psi_a(r_1)\psi_b(r_2) \pm \psi_a(r_2)\psi_b(r_1)}{\sqrt{2}} \tag{39}$$

The exchange of coordinates $r_1$ and $r_2$ in $\Psi_{spatial}(r_1, r_2) \rightarrow \Psi_{spatial}(r_2, r_1)$ will show the symmetry of the wavefunction. It is a symmetric spatial state if the positive sign remains after exchange (i.e. $\Psi_+(r_1, r_2) = \Psi_+(r_2, r_1)$), see **Eq. 40 & 41**) and antisymmetric for a change to negative sign (i.e. $\Psi_-(r_1, r_2) = -\Psi_-(r_2, r_1)$), see **Eq. 42 & 43**).

This is shown explicitly below:

Symmetric spatial state:

$$\Psi_+(r_1, r_2) = \frac{\psi_a(r_1)\psi_b(r_2) + \psi_a(r_2)\psi_b(r_1)}{\sqrt{2}} \tag{40}$$

Exchanged symmetric spatial state:

$$\Psi_+(r_2, r_1) = \frac{\psi_a(r_2)\psi_b(r_1) + \psi_a(r_1)\psi_b(r_2)}{\sqrt{2}} = \Psi_+(r_1, r_2) \tag{41}$$

Antisymmetric spatial state:

$$\Psi_-(r_1, r_2) = \frac{\psi_a(r_1)\psi_b(r_2) - \psi_a(r_2)\psi_b(r_1)}{\sqrt{2}} \tag{42}$$

Exchanged antisymmetric spatial state:

$$\Psi_-(r_2, r_1) = \frac{\psi_a(r_2)\psi_b(r_1) - \psi_a(r_1)\psi_b(r_2)}{\sqrt{2}} = -\Psi_-(r_1, r_2) \tag{43}$$

So far, we have only been dealing with the spatial part of the electron wavefunction. In reality, there is a spin component as well.

For two electrons, the spins can adopt a singlet state ($\chi_S$) with antiparallel spins or a triplet state ($\chi_T$) (parallel spins). Colloquially, $\alpha$ represents the up spin and $\beta$ for the down spin. Examples of the overall wavefunction (**Eq. 44 & 45**) are shown below for the singlet and triplet state:

$$\Psi_{singlet} = \Psi_+ \chi_S = \frac{\psi_a(r_1)\psi_b(r_2) + \psi_a(r_2)\psi_b(r_1)}{\sqrt{2}}(\alpha(1)\beta(2) - \alpha(2)\beta(1)) \quad \textbf{(44)}$$

$$\Psi_{triplet} = \Psi_- \chi_T = \frac{\psi_a(r_1)\psi_b(r_2) - \psi_a(r_2)\psi_b(r_1)}{\sqrt{2}}(\alpha(1)\beta(2) + \alpha(2)\beta(1)) \quad \textbf{(45)}$$

**3.8.2 The Energy of Coupling**

We will now show that the energy of the system is lowered when two spins are coupled together. The Hamiltonian between two spin 1/2 particles is given by **Eq. 46**:

$$\hat{H} = -2J\hat{S}_1 \cdot \hat{S}_2 \quad \textbf{(46)}$$

where $\hat{S}_1$ and $\hat{S}_2$ represent the operators for the two individual particle spins.

The expectation values for these wavefunctions can be calculated by **Eq. 47**:

$$\langle E_{singlet} \rangle = \int \Psi_{singlet}^* \hat{H} \Psi_{singlet} dr_1 dr_2 = \langle \Psi_{singlet}^* | \hat{H} | \Psi_{singlet} \rangle \quad \textbf{(47)}$$

Since the Hamiltonian only operates on the spatial parts of the wavefunction, the expectation value for the singlet state simplifies to **Eq. 48**:

$$\langle E_{singlet} \rangle = \langle \psi_a(r_1)\psi_b(r_2) + \psi_a(r_2)\psi_b(r_1) | \hat{H} | \psi_a(r_1)\psi_b(r_2) + \psi_a(r_2)\psi_b(r_1) \rangle \qquad \textbf{(48)}$$

The triplet state calculation proceeds similarly seen below in **Eq. 49** and **Eq. 50**:

$$\langle E_{triplet} \rangle = \int \Psi_{triplet}^{*} \, \hat{H}\Psi_{triplet} dr_1 dr_2 = \langle \Psi_{triplet}^{*} | \hat{H} | \Psi_{triplet} \rangle \qquad \textbf{(49)}$$

$$\langle E_{triplet} \rangle = \langle \psi_a(r_1)\psi_b(r_2) - \psi_a(r_2)\psi_b(r_1) | \hat{H} | \psi_a(r_1)\psi_b(r_2) - \psi_a(r_2)\psi_b(r_1) \rangle \qquad \textbf{(50)}$$

The coefficient (J, exchange constant or exchange integral) of the Hamiltonian in **Eq. 46** is precisely the difference between the singlet and triplet state divided by 2 (see **Eq. 51**):

$$J = \frac{\langle E_{singlet} \rangle - \langle E_{triplet} \rangle}{2} = \langle \psi_a(r_1)\psi_b(r_2) | \hat{H} | \psi_a(r_2)\psi_b(r_1) \rangle \qquad \textbf{(51)}$$

When $J$ is positive, $\langle E_{singlet} \rangle > \langle E_{triplet} \rangle$ so therefore the triplet state is more energetically favourable (S = 1). When $J$ is negative, then the singlet state is favoured with S = 0.

## 3.9 Itinerant Electrons

Within the localization paradigm, many observed phenomena can be explained. For example, Weiss' model of ferromagnetism is able to explain observed values of spontaneous magnetization and can also explain the existence of a paramagnetic phase transition (Curie-Weiss law). Localization runs into problems when it is applied to metals, since the electrons are able to freely travel throughout the lattice (thus resulting in high electrical conductivity) and are not localized at all. These delocalized electrons are called itinerant electrons. The localized theory is unable to explain, for example,

measured values of magnetic moment per atom for ferromagnetic metals (which are rational numbers rather than integer, a result predicted by localization). To fully capture the essence of magnetism in metals, we must introduce band theory which is entirely another school of thought.

In the solution of Schrodinger's equation it can be seen that electrons in a free atom may only occupy certain discrete energy levels. These are known as atomic orbitals. When atoms are brought into close proximity of each other, it is possible for the wavefunctions of the atomic orbitals to mix and overlap and create new energy levels. This usually happens between the atomic orbitals of the valence electrons since they stretch the furthest. When we consider solids, there are a large amount of neighboring atoms leading to energy levels that are very closely spaced and appear as an, almost, continuous band of energy levels (hence the name, band theory).

### 3.9.1 Free-electron Theory and Density of States

The free-electron theory is a model that assumes all valence electrons in a solid to be ionized and detached from their atoms which can freely wander in the solid. The electrostatic potential of these vagabond electrons are assumed to be 0; the forces from the ion cores as well as other electrons exactly cancel each other.

Schrodinger's equation for the free electron becomes (**Eq. 52**):

$$-\frac{\hbar^2}{2m}\left(\frac{\partial^2\Psi}{\partial x^2}+\frac{\partial^2\Psi}{\partial y^2}+\frac{\partial^2\Psi}{\partial z^2}\right)=E\Psi \tag{52}$$

Solutions to this equation require periodic boundary conditions and can be greatly simplified if the electrons are assumed to be within the confines of a cube with edge length L. With this assumption, solutions to the equation would take on the form of **Eq. 53**:

$$\Psi(r)=e^{ik\cdot r} \tag{53}$$

where $k$ represents a wavevector that has the values of $k_x, k_y, k_z = \pm\frac{2\pi n}{L}$ and $n$ is a positive integer. Substitution of the solution (**Eq. 53**) back into the original equation (**Eq. 52**) yields the energy eigenvalues (**Eq. 54**):

$$E=\frac{\hbar^2}{2m_e}(k_x{}^2+k_y{}^2+k_z{}^2) \tag{54}$$

The energy for a particular **k**-state is shown above. The Fermi energy $(E_F)$ is defined to be the energy level of the highest state occupied by electrons at 0K (**Eq. 55**).

$$E_F=\frac{\hbar^2}{2m_e}k_F{}^2 \tag{55}$$

where $k_F$ is the Fermi wavevector (wavevector of highest filled state). We can think of the Fermi wavevector as defining the radius of a sphere in **k**-space with volume $\frac{4}{3}\pi k_F{}^3$. By definition, our wavevector k is quantized in units of $\frac{2\pi}{L}$ meaning that is how much the electronic states are separated by. Each of the states may be doubly occupied and has a

volume of $\left(\frac{2\pi}{L}\right)^3$. We have all the necessary ingredients to calculate the total number of

electrons up to $E_F$ (**Eq. 56**).

$$N = \frac{\frac{4\pi k_F{}^3}{3}}{\left(\frac{2\pi}{L}\right)^3} \times 2$$

$$N = \frac{L^3 k_F{}^3}{3\pi^2}$$

$$N = \frac{L^3 \left(\frac{2m_e E_F}{\hbar^2}\right)^{\frac{3}{2}}}{3\pi^2} \tag{56}$$

Now that we have the total number of electronic states, we can find an

expression (**Eq. 57**) for the density of states, $D(E)$, which is simply $\frac{dN}{dE}$. This tells us how

many electron states there are for an energy range.

$$D(E_F) = \frac{dN}{dE} = \frac{L^3 \left(\frac{2m_e}{\hbar^2}\right)^{\frac{3}{2}} E_F^{\frac{1}{2}}}{2\pi^2} \tag{57}$$

which can be written succinctly as **Eq. 58**:

$$D(E_F) = \frac{3N}{2E_F} \tag{58}$$

Another useful expression that can express the density of states is **Eq. 59**:

$$D(E_F) = \frac{m_e k_F}{(\pi L)^2} \tag{59}$$

which shows that $D(E)$ is directly proportional to the mass of the electron. Many important physical properties are dependent on the density of states near the Fermi energy.

So far, the discussion of the density of states has focused on when T = 0 for the Fermi energy. When T > 0, the occupancy of each state can be represented by the Fermi-Dirac distribution (see **Figure 10**, **Eq. 60**), $f(E)$, and the density of states becomes the product of the two (**Eq. 61**):

$$f(E) = \frac{1}{e^{\frac{E-\mu}{k_B T}} + 1}$$ 

(60)

where $\mu$ is the chemical potential of the material.

For T > 0:

$$f(E)D(E)$$ 

(61)

For T = 0, analysis of the form of $f(E)$ shows that it is equal to 1 below $E_F$ and equal to 0 above, known as a type of step function (see **Figure 10**). The Fermi energy is equal to the chemical potential, $\mu$, which is defined to be the energy needed to add 1 particle to the system. The Fermi surface is known as the set of points in k-space where the energy is equal to the chemical potential.
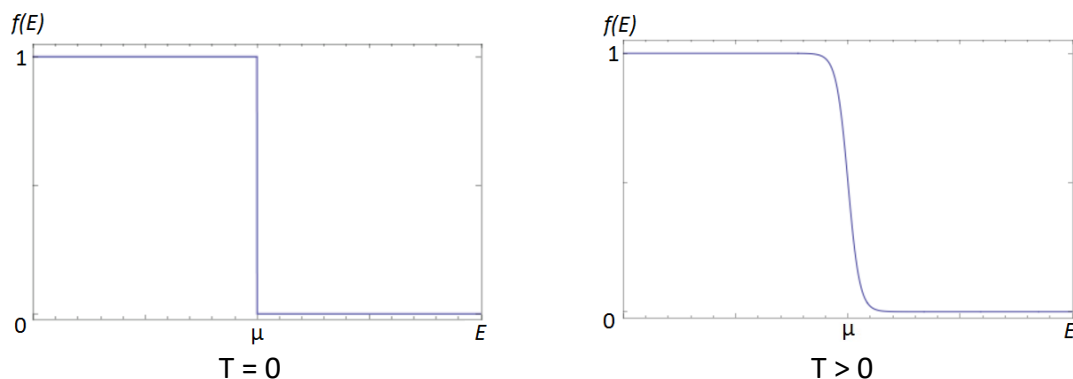
**Figure 10:** Fermi-Dirac distribution for T = 0 (left) and for T > 0 (right).

The density of states around the Fermi energy is particularly important because the shape of the function determines many properties in the solid. The Fermi surface is the threshold between all the occupied states and the empty states and is the region where excitations (thermal or magnetic) occur.

### 3.9.2 Pauli Paramagnetism

In equilibrium, each electronic state in a metal is occupied by two electrons, one with spin-up and the other with spin-down. With the application of a magnetic field, those electrons that have their magnetic moment parallel to the field will be lower in energy than the antiparallel electrons.

Say that the field is applied in the up direction. The negative charge of the electron makes the magnetic moment orient in the opposite direction of the spin so that electrons that are down-spin would have lower energy than those that are up-spin. In a density of states diagram, the electron band is said to be spin-split by the magnetic field into two subbands (see **Figure 11**).
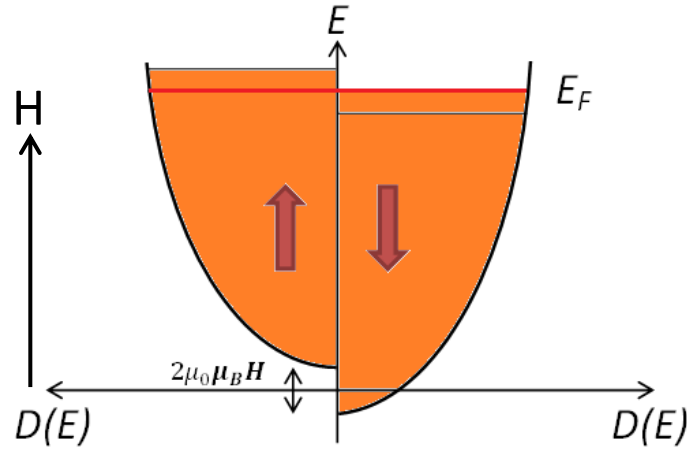
**Figure 11:** Density of states for a free electron gas in applied field. The field is applied in the up direction and is parallel to the down-spin magnetic moments.

Recall that for a free electron, the magnetic moment along the field direction is given by **Eq. 62**:

$$m_z = -gm_s\boldsymbol{\mu_B} = \pm\boldsymbol{\mu_B} \qquad \textbf{(62)}$$

And that the magnetic field changes the energy of the atomic moment by $\mu_0\boldsymbol{mH}cos\theta$. For an electron whose magnetic moment is parallel to the field (spin down moment), the energy will therefore be lowered by $\mu_0\boldsymbol{\mu_B}H$ $(\cos(180) = -1)$ with respect to $E_F$ while the energy for an electron whose magnetic moment is antiparallel will be raised $\mu_0\boldsymbol{\mu_B}H$ above $E_F$. To calculate the net magnetic moment, the difference between the number of down-spin electrons and the number of up-spin moments is multiplied by $\frac{\mu_B}{2}$ (**Eq. 63**). We must divide by a factor of two because the density of states was defined for two electrons per orbital. This integral is evaluated into **Eq. 64**.

$$m = \frac{\mu_B}{2} \int_{E_F - \mu_0 \mu_B H}^{E_F + \mu_0 \mu_B H} D(E) dE \tag{63}$$

$$m = \mu_0 \mu_B^2 H D(E_F) = \frac{3}{2} \mu_0 \mu_B^2 H \frac{N}{E_F} \tag{64}$$

To obtain the susceptibility of a Pauli paramagnet (**Eq. 65**), the magnetic moment per unit volume is divided by $H$:

$$\chi = \frac{3}{2} \mu_0 \mu_B^2 \frac{\frac{N}{V}}{E_F} \tag{65}$$

### 3.9.3 Itinerant Ferromagnetism

The Stoner model is based on the following postulates:

1) The effects of exchange are described by a molecular field term $(\lambda M)$.

2) Fermi statistics are used.

3) All the magnetic moments are located in the d-band.

Suppose that some of the electrons in the spin-down band are transferred to the spin-up band. What is the energy cost? This situation is similar to the one we encountered during Pauli paramagnetism but in this case, there is no external magnetic field (see **Figure 12**).
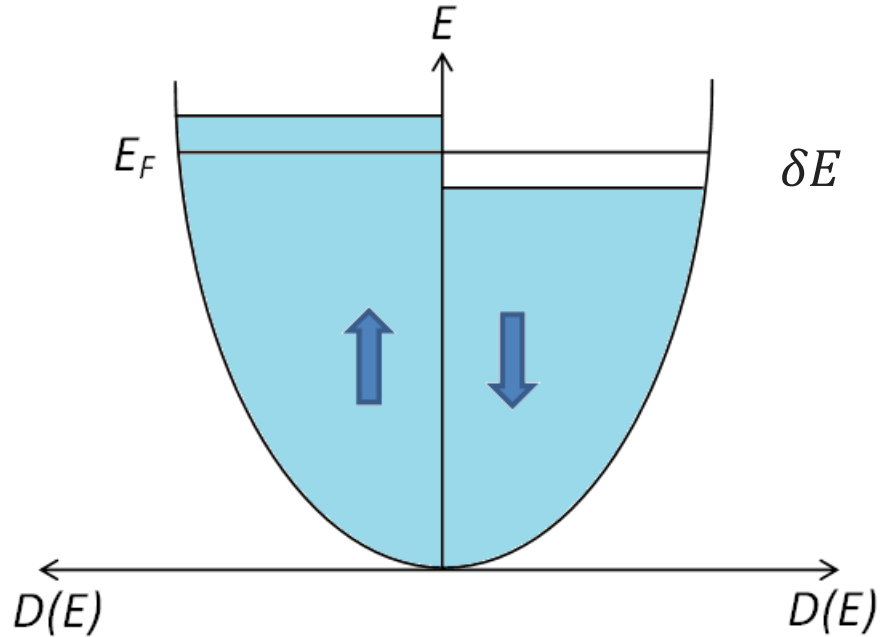
**Figure 12:** Density of states of free electron gas, spontaneously splitting, without applied magnetic field.

Spin-down electrons are taken from the region $[E_F - \delta E, E_F]$ and put into the spin-up region, $[E_F, E_F + \delta E]$. The number of electrons that are converted is given by **Eq. 66**:

$$\frac{D(E_F)(\delta E)}{2} \tag{66}$$

which all go up in energy by $\delta E$. Therefore, the total energy cost of changing the spin is shown in **Eq. 67**:

$$\Delta E_{kin} = \frac{1}{2} D(E_F)(\delta E)^2 \tag{67}$$

Whether or not the material will spontaneously become ferromagnetic is dependent on whether this energy cost can be outweighed by the energy gain from

reorienting the magnetic moments. The potential energy gain (**Eq. 68**) can be calculated by the following integral:

$$\Delta E_{pot} = -\int_0^M \mu_0 \left(\lambda M'\right) dM' = -\frac{1}{2}\mu_0 \lambda M^2 = -\frac{1}{2}\mu_0 \mu_B^2 \lambda \left(D(E_F)(\delta E)\right)^2 \qquad \textbf{(68)}$$

Therefore, the total energy change (**Eq. 69**) is:

$$\Delta E_{tot} = \Delta E_{kin} + \Delta E_{pot} = \frac{1}{2}D(E_F)(\delta E)^2 - \frac{1}{2}\mu_0 \mu_B^2 \lambda \left(D(E_F)(\delta E)\right)^2$$

$$\Delta E_{tot} = \frac{1}{2}D(E_F)(\delta E)^2 \left(1 - \mu_0 \mu_B^2 \lambda D(E_F)\right) \qquad \textbf{(69)}$$

In order for the system to order ferromagnetically, the total change in energy must be negative which is only possible when $\mu_0 \mu_B^2 \lambda D(E_F) \geq 1$ since $D(E_F)$ is positive, and $\delta E$ is squared (positive). This condition is known as the Stoner criterion. We can see that this condition is fulfilled when either $\lambda$ or the density of states at $E_F$ are very large. For most metallic systems, the molecular field constants do not vary much and are around the same order of magnitude therefore the key factor in determining the ferromagnetism of the material is the density of states at $E_F$.

## 3.10 Magnetocaloric Effect (MCE)

The MCE is an effect that is intrinsic in all materials and is the temperature difference that is obtained from applying a magnetic field. It describes the reversible process of converting the magnetic entropy stored within the system into heat. This

involves the adiabatic magnetization/demagnetization of the compound that results in a heating/cooling of the material.

The magnitude of this effect can be amplified in the case of ferromagnetic materials that have a structural change (first discovered in 1997[6]).

The degree of MCE can be evaluated from magnetization measurements to determine the isothermal entropy change $(\Delta S_{iso})$ which shows how much potential energy may be converted into heat.  The MCE may also be quantified from heat capacity measurements to determine the adiabatic temperature change $(\Delta T_{ad})$.

### 3.10.1 Thermodynamics of MCE

Entropy of the system can be written in the form of **Eq. 70**:

$$S(T)_{H,P} = \int\limits_{T\to 0}^{T} \frac{C(T)_{H,P}}{T}\, dT \tag{70}$$

In the case of a second-order phase transition, the isothermal entropy change equals (**Eq. 71**):

$$\Delta S_{iso}(T) = \int\limits_{T\to 0}^{T} \frac{C(T)_{H_2,P} - C(T)_{H_1,P}}{T}\, dT \tag{71}$$

The adiabatic temperature change (**Eq. 72**) indicates by how many degrees the material may be cooled under the influence of a field and is related to the isothermal entropy change:

$$\Delta T_{ad}(T) = -\frac{T \Delta S_{iso}(T)}{C(T)_{H_2,P}}$$  (72)

For a magnetocaloric material with a first-order phase transition, there is an associated structural transition that occurs at the same time as the magnetic phase transition. There is a finite amount of enthalpy that comes with the structural change that causes the entropy to become discontinuous and adds an extra term (see **Eq. 73**):

$$\Delta S_{iso}(T) = \int_{T \to 0}^{T} \frac{C(T)_{H_2,P} - C(T)_{H_1,P}}{T} dT - \frac{\Delta E_{H_1}}{T_{c1}}$$  (73)

In addition to the method of measuring heat capacity, it is also possible to derive the isothermal entropy change from magnetization measurements. Usually, the indirect method of calculating the magnetic entropy change is done by collecting isothermal magnetization curves above and below the transition temperature. The value $\Delta S_m$ can be evaluated from the Maxwell equation in **Eq. 74**:

$$\left(\frac{\partial S}{\partial H}\right)_T = \left(\frac{\partial M}{\partial T}\right)_H$$  (74)

Since discrete temperature intervals are used, numerical integration is used (**Eq. 75**):

$$\Delta S_m\,(T,H) = \int\limits_{H_i}^{H_f} (\frac{\partial M}{\partial T})_H dH \approx \sum_i \frac{M_i(T_{n+1},H) - M_i(T_n,H)}{T_{n+1} - T_n}\Delta H \qquad (75)$$

where $\Delta H$ is the field difference between magnetization measurements, and $M_i(T_{n+1},H)$ and $M_i(T_n,H)$ are the values of magnetization at the two temperatures $T_{n+1}$, $T_n$ respectively. The summation occurs over the magnetization values along two magnetic isotherms.

### 3.10.2 Magnetic Cooling

Adiabatic demagnetization is a technique that is capable of cooling samples via a magnetic field. Given a ferromagnetic sample at high temperatures (well above $T_c$), the magnetic moments will randomly point in all directions and have a 0 net magnetization. We can describe the magnetic part of the entropy through the following equation (**Eq. 76**):

$$S = k_B \ln W \qquad (76)$$

where $W = (2J + 1)^N$ is the number of microscopic configurations of the magnetic moments. In the case of an applied magnetic field and when the orbital angular momentum is quenched, then $J = S = \frac{1}{2}$ and $W = 2^N$ (magnetic moments are either parallel or antiparallel to the field). Therefore:

$$S = k_B \ln W = k_B \ln 2^N = N k_B \ln 2 \qquad (77)$$

We can see from **Eq. 77** that there is a finite amount of entropy. In the ferromagnetic state and the moments are fully aligned, $S = k_B \ln 1 = 0$. The magnetic entropy is lowered for the fully ordered state.

The process of magnetic cooling consists of two different steps: the adiabatic magnetization of the sample, and the adiabatic demagnetization of the sample.

The first step is to adiabatically magnetize the sample, meaning that the system is magnetized without any heat transfer between the system and the surrounding. As we saw above, when the system becomes fully ordered, the magnetic entropy decreases. The entropy of the whole system must be constant because of the adiabatic conditions, meaning the energy that was lost must manifest itself in another form in the sample. The magnetic energy is converted into thermal energy in the form of phonons (lattice vibrations). This translates into an increase of temperature. The generated heat is then removed into the surroundings to maintain the original temperature of the sample.

The second step is to take away the applied magnetic field adiabatically. When the moments start to become disordered, the magnetic entropy increases which is balanced out by a decrease in the phonon entropy. This leads to a decrease in temperature and we have achieved the process of magnetic cooling.

The potential benefits of these materials are big and plentiful. They can convert energy much more efficiently than current vapour-based cooling technology (60% vs. 40% Carnot efficiency)[7,8,9]. If the composition of the magnetocaloric material is selected carefully, we can choose earth abundant elements resulting in affordable manufacturing costs. In addition to being cheap, we can avoid toxic elements in the composition so that magnetocaloric materials can be environmentally friendly. The switch to magnetocaloric materials also eliminates the need for hazardous and ozone depleting compounds such as chlorofluorocarbons used in vapour compression technology making the environmental benefits even greater. Also, since we are dealing with solid materials, more compact cooling units can be fabricated.

The process of adiabatic demagnetization for magnetic cooling is currently used for cryogenic applications, however, has not yet crossed the barrier to commercialization.

**Chapter 4. Landau's Theory of Phase Transitions**

Phase transitions are points that are singularities in free energy. The calculation of free energy typically requires knowing the density of states of the system which is quite a laborious process. In his 1937 paper, Landau considered the nature of phase transitions from a symmetry point of view[10]. He realized that an approximate form of the free energy (as a power series) can always be established based on an order

parameter that is an important degree of freedom in the system. This order parameter has a value of 0 on the high temperature side of the phase transition and non-zero values on the low temperature side. For example, the order parameter could be chosen as magnetization for a paramagnetic to ferromagnetic phase transition.

Phase transitions can either be discontinuous (first-order) or continuous (second-order or critical). First-order phase transitions have discontinuous first derivatives of free energy with respect to intensive variables (e.g. entropy or volume is discontinuous) at the point of transition. Phase transitions of the second-order have a discontinuous second derivative of free energy and a continuous first derivative (such as heat capacity, or susceptibility). In the majority of $2^{nd}$ order phase transitions, the phase that exists at higher temperature will be more symmetrical than that of its lower temperature counterpart.

We will start with describing second-order phase transitions and then move into the first-order kind.

The theory is formed on the basis of a probability density function, $\rho(x, y, z)$ which gives the probability of finding an atom for a given volume. This function is invariant with respect to the symmetry of the crystal lattice and can be decomposed into a linear combination of $\varphi_i^n$ represented by **Eq. 78**:

$$\rho \ = \ \sum_{n} \sum_{i} c_i^n \varphi_i^n \tag{78}$$

where $\varphi_i^n$ represents the $i^{\text{th}}$ basis function for the $n^{\text{th}}$ irreducible representation of the space group, $c_i^n$ are constants. For any symmetry group $G_0$, if one chooses $\varphi_i^n$ to be the minimum number of functions needed to transform into combinations of each other by all of the symmetry transformations in $G_0$, this set is called an irreducible representation and can be used as a basis for the group. These functions have the unique property of being able to transform into combinations of each other through the symmetry elements of the space group.

Each of the symmetry operations in a given group can be represented in matrix form. For example, counterclockwise rotation around the z axis by angle $\theta$ is given by:

$$\begin{matrix} \cos\theta & -\sin\theta & 0 \\ \sin\theta & \cos\theta & 0 \\ 0 & 0 & 1 \end{matrix}$$

and therefore for a 90° rotation, the matrix would take the form:

$$\begin{matrix} 0 & -1 & 0 \\ 1 & 0 & 0 \\ 0 & 0 & 1 \end{matrix}$$

At the transition point, the probability density starts to change by a small amount, $\delta\rho$, and we can rewrite **Eq. 78** into **Eq. 79**:

$$\rho \;=\; \rho_0 \;+\; \delta\rho = \rho_0 \;+\; \sideset{}{'}\sum_{n}\sum_{i} c_i^{n}\varphi_i^{n} \qquad\qquad (79)$$

where the unit representation, $\rho_0$, represents the function that is invariant with respect

to all symmetry transformations of the space group. There is only one such function for

any symmetry group. The symmetry elements contained in the group, $\delta\rho$, is a subspace

of the group, $\rho_0$. This is evident since the highest symmetry term, $\rho_0$, was originally part

of the summation in **Eq. 78**.

If $\rho$ does not change under the symmetry transformations of the group $G_0$,

neither must the thermodynamic potential (e.g. Gibbs free energy)  of the system

because there was no change in the atomic structure.  The potential $(\Phi)$ takes on the

same symmetry and we can rewrite **Eq. 79** in terms of $\Phi$:

$$\Phi = \Phi_0 + \sideset{}{'}\sum_{n} \alpha^{(n)} \sum_{i}(c_i) + \cdots \qquad\qquad (80)$$

where in **Eq. 80**, $\alpha$ is a coefficient that is a function of the specific pressure and

temperature.  Compare this to **Eq. 79**, and we find that the symmetry group of the

crystal follows immediately after the determination of only the $c_i$.  This is because the

way the basis functions (of each irreducible representation) transform into each other is

known.

In this expansion, the coefficient $\alpha$ of the linear term should always equal to 0.

In other words, no linear terms can be unchanged from the symmetry transformations in

the irreducible representation. Furthermore, the two possibilities, $c_i = 0$ and $c_i \neq 0$ represent different symmetries and so the first order term must disappear yielding **Eq. 81**.

$$\Phi = \Phi_0 + \sum_n {}'A^{(n)} \sum_i (c_i)^2 + \cdots \tag{81}$$

At the point of phase transition, all $c_i$ must be equal to $0$ ($\Phi = \Phi_0$) and the symmetry of the crystal is $G_0$. It should be evident that all $A^{(n)}$ must be positive prior to the transition point, for if they were negative, then the potential would be a maximum at the phase transition instead of a minimum.

Once we cross the transition point, there are two possible cases: either the system retains or changes its symmetry. In the case where the system retains its symmetry, $c_i$ must stay equal to $0$ all the time. In the more interesting scenario when the system changes symmetry, $c_i \neq 0$, and the sign of one of the $A^{(n)}$ (belonging to the $n^{th}$ representation) must change to negative after the transition. This symbolizes the appearance of an irreducible representation which changes the symmetry of the system. The rest of the coefficients $A^{(n)}$ stay positive near the transition point and their corresponding $c_i$ are still $0$.

The symmetry of the new structure belongs to this single irreducible representation and we can rewrite the summation to be over the basis functions of the one irreducible representation and in terms of the order parameter $\eta$ (**Eq. 82**).

$$\sum_i (c_i)^2 = \eta^2, \qquad c_i = \eta \gamma_i \tag{82}$$

The expression of $\Phi$ then becomes **Eq. 83**:

$$\Phi = \Phi_0 + A\eta^2 + \eta^3 \sum_\alpha B_\alpha f_\alpha^3(\gamma_i) + \eta^4 \sum_\alpha C_\alpha f_\alpha^4(\gamma_i) + \cdots \tag{83}$$

where $f_\alpha^3(\gamma_i)$, $f_\alpha^4(\gamma_i)$ are 3$^{rd}$ and 4$^{th}$ order invariants, $B_\alpha$ and $C_\alpha$ are coefficients, and $\alpha$ is

the number of independent invariants of the corresponding order. Similar to the linear

term, the third-order term must disappear (coefficients of higher odd-order powers are

also 0) because it cannot stay invariant with respect to the symmetry transformations in

$G_0$. For second-order phase transitions to occur, the second-order term must change

from positive to negative and the fourth-order terms must stay positive. The expansion

can be simply written as **Eq. 84**:

$$\Phi = \Phi_0 + A\eta^2 + \eta^4 \sum_\alpha C_\alpha f_\alpha^4(\gamma_i) + \cdots \tag{84}$$

For simplicity, the above equation can be written as the final form in **Eq. 85**:

$$\Phi = \Phi_0 + A\eta^2 + C\eta^4 + E\eta^6 + \cdots \tag{85}$$

The system will undergo a first-order phase transition if $A, E > 0$ and $C < 0$. In this

case, a state is possible at which two structures are at equilibrium ($\eta = 0, \eta \neq 0$). A

summary is given in **Figure 13**.

$$\Phi - \Phi_0$$

Before Transition

$$A, C, E > 0$$

1st order

2nd order

$$\Phi - \Phi_0$$

After Transition

$$A, E > 0 \text{ and } C < 0$$

$$\Phi - \Phi_0$$

After Transition

$$C, E > 0 \text{ and } A < 0$$
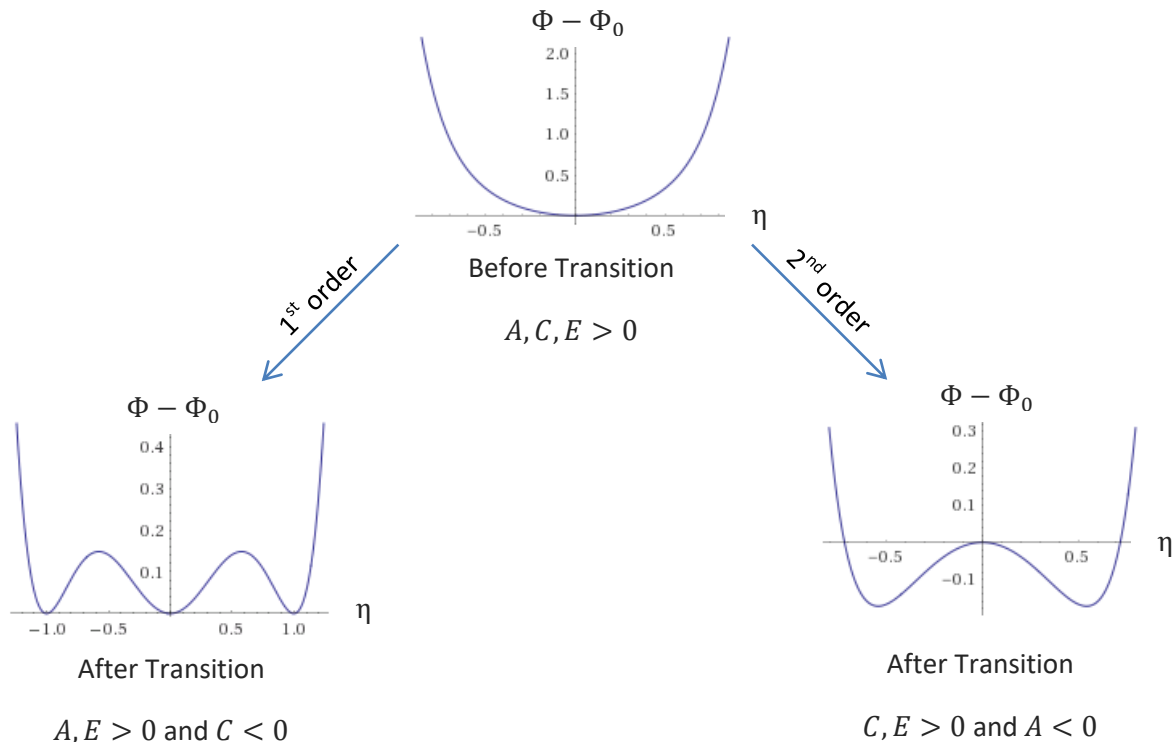
**Figure 13**: Thermodynamic potential before (top) and after a first-order phase transition (left) and second-order phase transition (right). For the first-order phase transition, we can see that two structures are in equilibrium for $\eta = 0$ and $\eta = \pm 1$. For the second-order phase transition, there exists only one structure at equilibrium at a time. It is a continuous transition from the high symmetry structure before the transition, to the lower symmetry structure after.

## 4.1 Applications to Magnetic Phase Transitions

In particular, Landau's theory can also be applied to second-order magnetic phase transitions. The potential, $\Phi$, of an ideal ferromagnetic material that is isotropic and single domain can be expanded as a power series of magnetization $(\text{M})$.

If there is no external magnetic field, the expansion will take the form of **Eq. 86**:

$$\Phi = \Phi_0 + A\text{M}^2 + C\text{M}^4 \dots \tag{86}$$

where $\Phi_0$ represents the potential that is invariant with respect to the symmetries of magnetization, and $A$ and $C$ are the thermodynamic coefficients.

At the transition temperature $(T = T_c)$, $A$ becomes 0 and negative for $T < T_c$ and can therefore be represented as **Eq. 87**:

$$A = A_0(T - T_c) \tag{87}$$

If we consider the influence of an external magnetic field, the potential (expanded to 4<sup>th</sup> order) becomes of the form seen in **Eq. 88**:

$$\Phi = \Phi_0 + A\mathrm{M}^2 + C\mathrm{M}^4 - H\mathrm{M} \tag{88}$$

where $H$ is the applied magnetic field. The symmetry of the system is broken with the inclusion of the field dependence term which describes the decrease in potential when the magnetic moments align with the field. Minimization of this equation (**Eq. 89**) describes the magnetization close to $T_c$:

$$\frac{\partial \Phi}{\partial M} = 0 = AM + CM^3 - H$$

$$\frac{H}{M} = A + CM^2 \tag{89}$$

Plugging in **Eq. 87** into **Eq. 89,** we obtain the relation **Eq. 90**:

$$\frac{H}{M} = A_0(T - T_c) + CM^2 \tag{90}$$

In order to determine the nature of a phase transition for a given sample, we can examine Arrott plots (see **Figure 14**) which show $M^2$ vs. $\frac{H}{M}$. From **Eq. 87**, when $T = T_c$ the first term of the equation disappears and therefore the isothermal curve that has no intercept would correspond with the critical temperature.
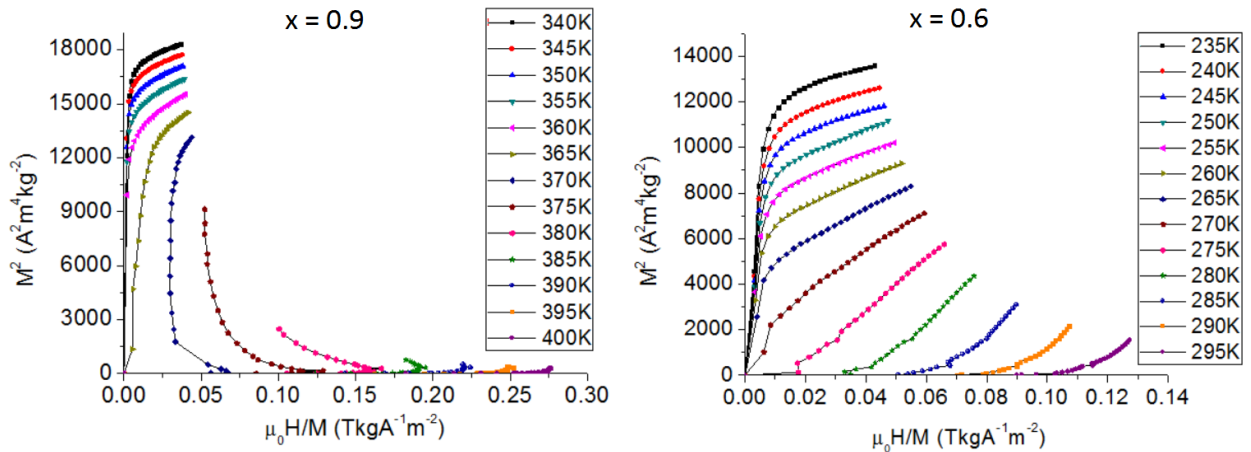


**Figure 14**: The Arrott plots for two samples in the $Mn_{2-x}Fe_xSi_{0.5}P_{0.5}$ (x = 0.9, 0.6) system are shown. Figure is taken from He, Svitlyk, Mozharivskyj[12].

For each sample x = 0.9 and x = 0.6, we see that the respective Curie temperatures derived from the Arrot plots seem to be 365K and 270K. The discrepancy between $T_c$ derived here and from magnetization data (see **Chapter 5.4.3**) could stem from the existence of thermal hysteresis (determined to be 6K for x = 0.9, virtually none for x = 0.6), resolution of the measurements (5K steps), and the time allowed for equilibrium. One thing to notice about the shape of the isothermal curves is the S-shaped behaviour which appears in both samples and is characteristic of first-order phase transitions.

## References

(1) West, A. R. *Solid State Chemistry and its Applications, 2$^{nd}$ ed.* John Wiley & Sons Ltd: Chichester, United Kingdon, **2014**.

(2) Pecharsky, V. K.; Zavalij, P. Y. *Fundamentals of Powder Diffraction and Structural Characterization of Materials*. Springer Science and Business Media, Inc: New York, U. S. A., **2009**.

(3) Spaldin, N. A. *Magnetic Materials Fundamentals and Applications, 2$^{nd}$ ed.* Cambridge University Press, New York, U. S. A., **2011**.

(4) Blundell, S. *Magnetism in Condensed Matter*. Oxford University Press Inc: New York, U.S.A., **2001**.

(5) Tishin, A. M.; Spichkin, Y. I. *The Magnetocaloric Effect and its Applications.* Institute of Physics Publishing: Bristol and Philadelphia, **2003**.

(6) Pecharsky, V. K.; Gschneidner, K. A., Jr. Giant Magnetocaloric Effect in Gd$_5$(Si$_2$Ge$_2$). *Phys. Rev. Lett.* **1997**, *78*, 4494 – 4497.

(7) Engelbrecht, K.; Nellis, G. F.; Klein, S. A. Zimm, C. B. Recent Developments in Room Temperature Active Magnetic Regenerative Refrigeration. *HVAC&R Research*. **2007**, *13*, 525.

(8) Pecharsky, V. K.; Gschneidner, K. A. Jr. Thirty years of near room temperature magnetic cooling: Where we are today and future prospects. *Int. J. Refrig.* **2008**, *31*, 945.

(9) Zimm, C.; Jastrab, A.; Sternberg, A.; Pecharsky, V. K.; Gschneidner, K. A. Jr.; Osborne, M.; Anderson, I. Description and Performance of a Near-Room Temperature Magnetic Refrigerator. *Adv. Cryog. Eng.* **1998**, *43*, 1759.

(10) Landau, L. Theory of Phase Transformations. I. *Zh. Eksp. Teor. Fiz.* **1937**, *7*, 19 – 32.

(11) Landau, L.; Lifshitz, E. *Statistical physics*. Addison-Wesley Publishing Company, INC: Massachusetts, U.S.A., **1958**.

(12) He, A.; Svitlyk, V.; Mozharivskyj, Y. Synthetic Approach for (Mn,Fe)$_2$(Si,P) Magnetocaloric Materials: Purity, Structural, Magnetic, and Magnetocaloric Properties. *Inorganic Chemistry*. **2017**, 56, 2827-2833.

**Chapter 5. Synthetic Approach for the (Mn,Fe)$_2$(Si,P) Magnetocaloric Materials: Purity, Structural, Magnetic and Magnetocaloric Properties**

**Abstract**

A conventional solid-state approach has been developed for synthesis of the phase-pure magnetocaloric Mn$_{2-x}$Fe$_x$Si$_{0.5}$P$_{0.5}$ materials (x = 0.6, 0.7, 0.8, 0.9).  Annealing at high temperatures followed by dwelling at lower temperatures is essential to obtain pure samples with x = 0.7, 0.8 and 0.9. Structural features of the samples with x = 0.6 and 0.9 were analyzed as a function of temperature via synchrotron powder diffraction. Curie temperatures, temperature hysteresis and magnetic entropy change were established from the magnetic measurements. According to the diffraction and magnetization data, all samples undergo a first-order magnetostructural transition but the first-order nature becomes less pronounced for Mn-richer samples.

**Introduction**

The discovery of magnetocaloric research can been credited to the great William Thomson in the late 1800s[1,2] when he correctly predicted that Fe, Ni, and Co would experience a cooling effect when removed from a magnetic field. Weiss and Piccard (nearly 60 years later) made the first known documented observation of the magnetocaloric effect (MCE) when they noticed a small temperature change in Ni[3] around its Curie temperature (T$_c$) upon application of a magnetic field.  After the discovery of this exotic phenomenon, there were only few practical uses for it mainly

because of the limitations in the operational temperatures and weak cooling power. One application that is still being used today is the attainment of cryogenic temperatures. In February 2016, Japan and the US jointly launched a new X-ray astronomy satellite, ASTRO-H (renamed to Hitomi), and a soft x-ray spectrometer (SXS) onboard is cooled to around -273.1°C by adiabatic demagnetization.[4] This cooling method is not new. The adiabatic demagnetization of a paramagnetic salt, $Gd_2(SO_4)_2 \cdot 8H_2O$, reached a temperature of 0.25K[5] in 1933.

In 1976, Brown from NASA constructed a Gd-containing magnetic refrigerator operating at room temperature[6] thus proving that magnetic cooling is a viable technique. It was not until 1997 that interest in magnetocaloric materials was revitalized due to the discovery of the giant magnetocaloric effect (GMCE) in the $Gd_5(Si,Ge)_4$ phases by Pecharsky and Gschneidner[7]. The $Gd_5(Si,Ge)_4$ phases exhibit a first-order magnetostructural phase transition; a first-order structural change coincides with the ferromagnetic to paramagnetic (FM-PM) magnetic transition and makes the MCE increase in magnitude.[8]

Such enhancement makes magnetic cooling an attractive alternative to the vapor-based techniques. Additionally, magnetic refrigerators have lower noise and smaller environmental impact. Ever since the 1997 discovery, the search was underway for materials capable of exhibiting the GMCE while being environmentally friendly and cheap. A few families of materials were discovered that possess first-order phase

transitions and GMCE. Among them are the $La(Fe_{1-x}Si_x)_{13}$ system reported by Hu *et al.*[9,10], the $MnAs_{1-x}Sb_x$ one researched by Wada *et al.*[11,12], and $Fe_2P$-type materials[13-15] which permits substitution of Mn for Fe and As or Ge for P.

This current work focuses on one of the most promising GMCE systems, the $Mn_{2-x}Fe_xSi_{0.5}P_{0.5}$ series. Compared to other $Fe_2P$-type materials, the $Mn_{2-x}Fe_xSi_{0.5}P_{0.5}$ phases do not contain expensive Ge or toxic As, instead they incorporate cheap and abundant Si. A first-order magnetostructural phase transition is preserved for this substitution. Upon cooling, the transformation features an abrupt change in the lattice parameters (without change in the symmetry) concomitant with a paramagnetic-to-ferromagnetic ordering at $T_C$. The low cost and abundance of starting materials along with easy tunability of $T_c$ make $Mn_{2-x}Fe_xSi_{0.5}P_{0.5}$ a desirable system to explore. This system crystallizes in the $P\bar{6}2m$ space group with two metal sites, 3f and 3g. The 3f site has been determined to be predominately Mn, which is surrounded by Si/P atoms in square pyramidal geometry while the 3g site is predominately occupied by Fe having a tetrahedral geometry of Si/P atoms around the metal center.[17]

While a significant amount of work has already been done on these materials, some questions remain unanswered such as the true values of $T_C$, magnetic entropy change, and hysteresis. The transition temperatures reported in the literature vary from $332K$[16] to $382K$[17] for $MnFeSi_{0.5}P_{0.5}$. Furthermore, the reported $T_C = 272K$[18] and thermal hysteresis of $\Delta T = 5K$[18] for $Mn_{1.3}Fe_{0.7}Si_{0.5}P_{0.5}$ also differs from those obtained in this work.

The primary synthetic technique for the $Fe_2P$-based materials has been ball-milling followed by sintering[13-16,18-21], however impurities such as cubic $(Mn,Fe)_3Si$ are common[16,20,21]. A more involved process, namely a drop synthesis in a high frequency induction furnace[17,22,23], can also be used to prepare these phases. Presented here is a new synthetic method capable of obtaining phase pure samples. It features a conventional solid-state approach that is reproducible and impurity-free.

**Experimental**

*Synthesis of $Mn_{2-x}Fe_xSi_{0.5}P_{0.5}$*

Stoichiometric amounts of Mn chunks (99.9 wt.%, Alfa Aesar), Fe granules (99.98 wt.%, Alfa Aesar), and Si lumps (99.999 wt.%, Alfa Aesar) were arc-melted together using a standard DC mono-arc welder. The total mass of each $Mn_{2-x}Fe_xSi_{0.5}P_{0.5}$ sample was 3 grams. Prior to melting, Mn chunks were washed in dilute nitric acid (5 wt.%) to remove the oxide layer from the surface. Elements were loaded into the arc-melting chamber on a water-cooled copper hearth, evacuated, and flushed with Ar gas (>99.999%). Direct exposure of Mn to the arc resulted in significant mass losses due to its relatively large vapour pressure. Placing Mn chunks under the Si and Fe pieces and slowly melting the latter produced samples with the highest yield. A small addition of extra Mn (~7mg) was necessary to counteract inevitable losses of Mn. The ingot obtained was flipped and

remelted several times to ensure homogeneity.  The mass of the samples was checked

after arc-melting and the total mass was within 0.1% from the target mass.

The samples were taken into a glovebox (Ar atmosphere, <0.1 $O_2$ ppm, <0.1 $H_2O$

ppm) where they were crushed into a fine powder and mixed thoroughly with red P

powder (99.5 wt.% CERAC Specialty Inorganics).  The mixtures were pressed into 10 mm

diameter pellets and sealed in evacuated silica tubes. The samples were heated to 270°C

at 50°C/h, kept for 12h, heated up to 1050°C at 100°C/h, annealed for 1 week and then

quenched in cold water.  To further improve sample homogeneity, the sintered samples

were reground, repressed, sealed in evacuated silica tubes, heated to 1050°C at 100°C/h

and annealed for 1 week.  After second annealing, $Mn_{2-x}Fe_xSi_{0.5}P_{0.5}$ samples with x = 0.7,

0.8, 0.9 had to be cooled to 400°C and then quenched in cold water to obtain phase

pure samples, while samples with x = 0.6 could be directly quenched from 1050°C.

Sample ampoules that were heated up too quickly cracked, likely due to the high vapour

pressure of P.  To avoid this problem, larger silica tubes were used and additionally, the

dwelling at 270°C for 12 hours was introduced before heating to 1050°C.

*Powder X-ray Diffraction (PXRD) and Synchrotron Studies*

Experimental PXRD data were collected from 2θ = 20°-70° on a PANalytical X'Pert

Pro diffractometer with a linear X'Celerator detector using $CuK\alpha_1$ radiation at room

temperature.  Phase analysis and refinement of the lattice parameters were performed

using the Rietveld technique with the Rietica software[24]. Temperature dependent powder diffraction data for the samples with x = 0.9 (277K - 424K) and x = 0.6 (201K - 500K) were collected at the European Synchrotron Radiation Facility, Grenoble, France; 2θ = 10°-51°, λ = 0.6999 Å.

*Magnetic Property Measurements*

Mass magnetization data were collected for the polycrystalline (x = 0.6, 0.7, 0.8, 0.9) samples on a Quantum Design SQUID MPMS magnetometer between 5 and 400K with steps of 5K and applied field of 100 Oe. To obtain a thermal hysteresis loop, magnetization was measured on cooling from 400K to 5K and then on heating to 400K. The isothermal entropy change was derived using the Maxwell relation:

$$\left(\frac{\partial M}{\partial T}\right)_H = \left(\frac{\partial S}{\partial H}\right)_T$$

from magnetic isotherms (ΔH = 5T in 2 kOe steps) measured in a 60K window around the Curie temperature with 5K steps. Calculation of the isothermal entropy change was done based on the magnetization values collected during heating. Before recording an M vs. H isotherm, the sample was heated up into the paramagnetic regime and then cooled to the targeted temperature for measurements. Heating above the Curie temperature eliminated any remnant magnetization that might have existed in the

sample. Ramping and cooling rate for all magnetization measurements were done at 10K/min.

Integration of the left side of the Maxwell equation over a change in the magnetic field, H, yields the equation below. In practice, a numerical integration is used due to the discrete temperature intervals:

$$\Delta S(T,H) = \int_{H_i}^{H_f} \left(\frac{\partial M}{\partial T}\right)_H dH \approx \sum_i \frac{M_i(T_{n+1},H) - M_i(T_n,H)}{T_{n+1} - T_n} \delta H$$

**Results and Discussion**

*Heating Trend and Sample Purity of Mn$_{2-x}$Fe$_x$Si$_{0.5}$P$_{0.5}$*

Samples with x = 0.7, 0.8, 0.9 and a Curie temperature above room temperature had to be cooled from 1050°C to 400°C and annealed at 400°C before quenching to ensure phase purity. The sample with x = 0.6 could maintain a single phase composition after being quenched directly from the annealing temperature of 1050°C. Based on these results, we can speculate that the simultaneous existence of the high- and low-temperature phases for x = 0.7, 0.8, 0.9 after quenching from 1050°C originates from a more uniform Mn/Fe mixing on the metal 3$f$ and 3$g$ sites. Due to the entropy contribution of the Gibbs free energy, the Mn/Fe occupancies on the 3$f$ and 3$g$ sites at the annealing temperature of 1050°C will be more equal than at the annealing temperature of 400°C. While quenching from 1050°C will allow some changes in the

Mn/Fe occupancy, the redistribution level will be much smaller than after subsequent annealing at 400$^o$C. Previous neutron diffraction data did support preferential occupancy of the 3$f$ site with Mn and 3$g$ site with Fe[17], however the dependence of site occupancies on annealing temperature was not studied. Our preliminary results suggest that the site occupancy is sensitive to the final annealing temperature and that the ferromagnetic low-temperature phase can only exist for distinct Mn/Fe ratios; more specifically a larger Fe/Mn segregation between the 3$f$ and 3$g$ sites, achieved via low-temperature annealing, leads to pure ferromagnetic samples with x = 0.7, 0.8, 0.9. However, it is not clear what Mn/Fe distribution on the two metal sites is required for the ferromagnetic phase to be form or what annealing temperatures besides 400$^o$C can achieve such distribution.

*Structural Changes*

Synthetic methods involving ball-milling yield small amounts of a secondary phase, $(Mn,Fe)_3Si$[16,20,21], which could alter the magnetic properties and lattice parameters of the main $(Mn,Fe)_2(Si,P)$ phase. Specifically, the $(Mn,Fe)_3Si$ impurity might affect several parameters: the composition of the main phase due to metal and/or Si deficiency; the lattice parameters of the main phase and degree of their change across the phase transition; related changes in the Curie temperature, magnetic entropy, and thermal hysteresis. The synthetic route reported in this paper yields completely pure samples and thus the physical parameters obtained can be seen as intrinsic for a given

composition. Temperature-dependant synchrotron data combined with magnetization data indicate the occurrence of a first-order coupled magnetostructural transition for the $Mn_{2-x}Fe_xSi_{0.5}P_{0.5}$ phases with $0.6 \leq x \leq 0.9$. The structural parameters and their changes will be discussed first followed by analysis of the magnetic properties.
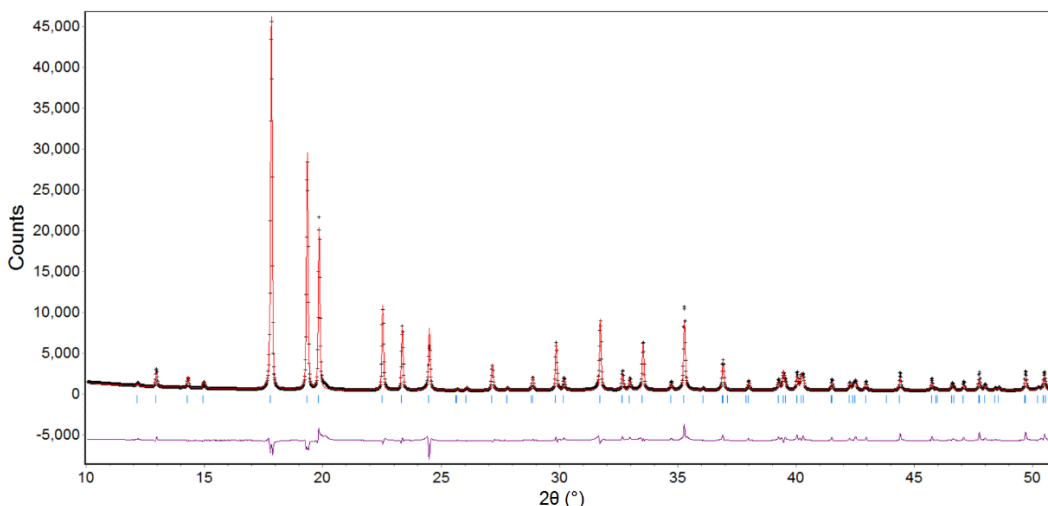


**Figure 15**: Rietveld refinement of the synchrotron data for $Mn_{1.1}Fe_{0.9}Si_{0.5}P_{0.5}$ at 298 K and $\lambda = 0.6999$ Å.

**Table 3**: Crystal parameters for $Mn_{2-x}Fe_xSi_{0.5}P_{0.5}$ at 298K.

| $Mn_{2-x}Fe_xSi_{0.5}P_{0.5}$ | a/b (Å) | c (Å) | Vol. (Å$^3$) |
|---|---|---|---|
| $Mn_{1.1}Fe_{0.9}Si_{0.5}P_{0.5}$ (x = 0.9) | 6.2044(1) | 3.2988(1) | 109.974(5) |
| $Mn_{1.2}Fe_{0.8}Si_{0.5}P_{0.5}$ (x = 0.8) | 6.1867(4) | 3.3225(3) | 110.13(1) |
| $Mn_{1.3}Fe_{0.7}Si_{0.5}P_{0.5}$ (x = 0.7) | 6.1538(6) | 3.3567(4) | 110.09(2) |
| $Mn_{1.4}Fe_{0.6}Si_{0.5}P_{0.5}$ (x = 0.6) | 6.1365(1) | 3.4062(1) | 111.080(5) |

The powder diffraction data revealed all $Mn_{2-x}Fe_xSi_{0.5}P_{0.5}$ samples to be single phase with no traces of impurities. A representative diffraction pattern and the Rietveld refinement for $Mn_{1.1}Fe_{0.9}Si_{0.5}P_{0.5}$ (x = 0.9) is shown in **Figure 15**. The Bragg peaks are indicated with blue ticks and can be assigned to the $Fe_2P$-type phase. In agreement with

literature data[17,20], all the phases crystallize with the $P\bar{6}2m$ space group. Lattice parameters for different Mn/Fe ratios (x = 0.6, 0.7, 0.8, 0.9) are summarized in **Table 3**. A larger Mn content leads to a decrease in the $a$ parameter and an increase in the $c$ parameter. The cell volume increases with the Mn amount, which is due to the larger atomic radius of Mn.
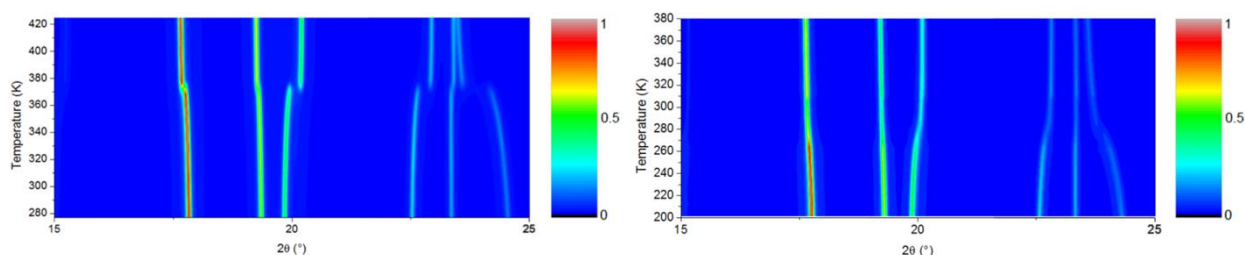


**Figure 16**: Temperature-dependent synchrotron diffraction data (15° - 25°) for $Mn_{1.1}Fe_{0.9}Si_{0.5}P_{0.5}$ (left) and $Mn_{1.4}Fe_{0.6}Si_{0.5}P_{0.5}$ (right).

Contour plots of the temperature-dependent synchrotron diffraction data for $Mn_{1.1}Fe_{0.9}Si_{0.5}P_{0.5}$ and $Mn_{1.4}Fe_{0.6}Si_{0.5}P_{0.5}$ are shown above in **Figure 16**. For clarity, only the 2θ range of 15° – 25° is presented. For $Mn_{1.1}Fe_{0.9}Si_{0.5}P_{0.5}$, the data clearly display a discontinuous change in the 2θ diffraction angles and coexistence of two phases near transition temperature, which are two features indicative of a first-order transition. On the other hand, the nature of the structural transition for $Mn_{1.4}Fe_{0.6}Si_{0.5}P_{0.5}$ is not so clear. At first glance, the gradual change in the 2θ angles suggests a second-order transition. However, the diffraction peak on the far right shows a discontinuous change, hinting at the possibility of a first-order transition. The first-order nature of $Mn_{1.4}Fe_{0.6}Si_{0.5}P_{0.5}$ is supported by a large magnitude of the magnetocaloric effect and by the Arrott plots derived from magnetization data (see the discussion below).

The synchrotron diffraction data for $Mn_{1.1}Fe_{0.9}Si_{0.5}P_{0.5}$ and $Mn_{1.4}Fe_{0.6}Si_{0.5}P_{0.5}$ allow visualization of the changes in lattice parameters and fractional coordinates for the two metal $3f$ ($x_1$, 0, 0), $3g$ ($x_2$, 0, 0.5) sites as a function of temperature (**Figure 17-18**, **Table 4**). The Fe/Mn occupancies used for refinement were based on previous neutron diffraction studies by Höglin et al.[17], who showed that Mn predominantly sits in the $3f$ site the 0.9228(2) occupancy, while Fe prefers the $3g$ site with the 0.9412(4) fraction. For the Rietveld refinements of $Mn_{1.1}Fe_{0.9}Si_{0.5}P_{0.5}$ and $Mn_{1.4}Fe_{0.6}Si_{0.5}P_{0.5}$, we assumed that Mn fully occupies the $3f$ site and the extra Mn goes into the $3g$ site along with Fe. Similar to the literature data, the crystal symmetry remains the same but lattice parameters change across the transition. The change in unit cell volume for $Mn_{1.1}Fe_{0.9}Si_{0.5}P_{0.5}$ is rather interesting (**Figure 17**, middle). Just below the Curie temperature the unit cell volume decreases sharply, then jumps up across the transition, and finally relaxes. Such behavior is an example of divergence/discontinuity at the transition temperature. The transition temperatures derived from the diffraction data are 373 and 276 K for $Mn_{1.1}Fe_{0.9}Si_{0.5}P_{0.5}$ and $Mn_{1.4}Fe_{0.6}Si_{0.5}P_{0.5}$, respectively. These temperatures differ somewhat from the Curie temperatures of 370 and 267K, which can be due to the fact that different experimental techniques with different temperature resolutions and heating rates were used.
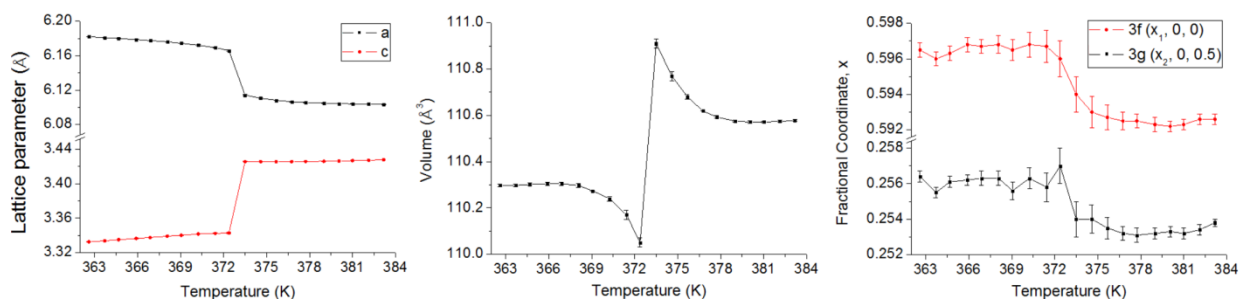
**Figure 17**: Lattice parameters, unit cell volume, and fractional coordinate, x, for the 3*f* and 3*g* sites in $Mn_{1.1}Fe_{0.9}Si_{0.5}P_{0.5}$ as a function of temperature (only 20 K interval around $T_C$ is shown).



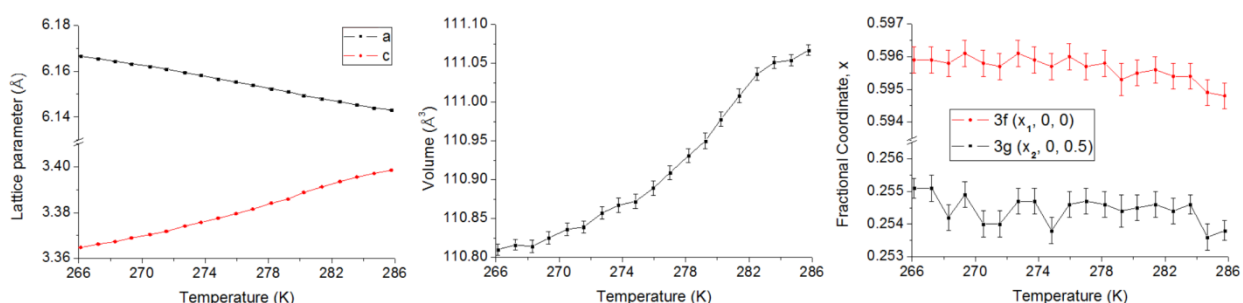**Figure 18**: Lattice parameters, unit cell volume, and fractional coordinate, x, for the 3*f* and 3*g* sites in $Mn_{1.4}Fe_{0.6}Si_{0.5}P_{0.5}$ as a function of temperature (only 20 K interval around $T_C$ is shown).

**Table 4**: Crystallographic and structural parameters of the paramagnetic (PM) and ferromagnetic (FM) phases for $Mn_{1.1}Fe_{0.9}Si_{0.5}P_{0.5}$ and $Mn_{1.4}Fe_{0.6}Si_{0.5}P_{0.5}$ across the transition temperature. Refinement was based on Mn fully occupying the 3*f* site and with extra Mn going into the 3*g* site together with Fe.

| Composition | Magnetic State and T | a/b (Å) | c (Å) | Volume (Å$^3$) | 3*f* (x$_1$, 0 , 0) | 3*g* (x$_2$, 0, 0.5) |
|---|---|---|---|---|---|---|
| $Mn_{1.1}Fe_{0.9}Si_{0.5}P_{0.5}$ | FM (363 K) | 6.1820(2) | 3.3325(1) | 110.297(5) | 0.5965(4) | 0.2564(3) |
| $Mn_{1.1}Fe_{0.9}Si_{0.5}P_{0.5}$ | PM (383 K) | 6.1034(1) | 3.4278(1) | 110.577(4) | 0.5926(3) | 0.2538(2) |
| $Mn_{1.4}Fe_{0.6}Si_{0.5}P_{0.5}$ | FM (266 K) | 6.1666(2) | 3.3648(2) | 110.810(7) | 0.5959(4) | 0.2551(3) |
| $Mn_{1.4}Fe_{0.6}Si_{0.5}P_{0.5}$ | PM (286 K) | 6.1431(2) | 3.3985(1) | 111.067(7) | 0.5948(4) | 0.2538(3) |

According to the Rietveld refinement, the fractional coordinates for the two metal sites decrease with increasing temperatures for both $Mn_{1.1}Fe_{0.9}Si_{0.5}P_{0.5}$ and $Mn_{1.4}Fe_{0.6}Si_{0.5}P_{0.5}$ (**Figure 17** and **Figure 18**, right), with the changes being more pronounced for $Mn_{1.1}Fe_{0.9}Si_{0.5}P_{0.5}$, which will be the only sample discussed. The atomic shifts combined with the variations in the lattice parameters allow visualization of

interatomic distances as a function of temperature. We will focus only on the metal-metal bonds as they have been shown to affect the magnetic interactions and transition temperature[21]. **Figure 19** presents the two shortest intraplanar and interplanar distances. For discussion purposes, we assume that the 3$g$ site is occupied only with Fe. As temperature increases, both the intraplanar Fe-Fe and Mn-Mn distances decrease while the two interplanar Fe-Mn distances slightly increase (see **Figure 20** and **21** for bond visualization). These changes imply that the paramagnetic state is favoured when intraplanar metal-metal distances are shorter and the interplanar ones are larger. The data also suggest that intraplanar distances are likely have a larger effect on the magnetic interaction then interplanar ones, since the intraplanar bonds vary more significantly. However, the increase in the interplanar distances cannot be ignored. As the interplanar distances grow, adjacent planes containing metal atoms become more separated and the ferromagnetic coupling becomes less stable. At $T_C$, the magnetic interactions break down and a paramagnetic state emerges.
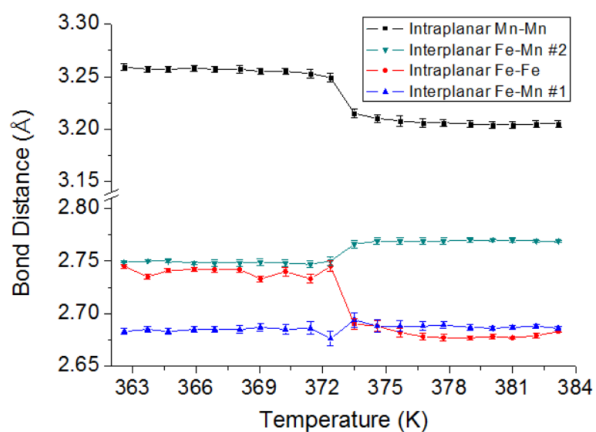


**Figure 19**: Metal-metal bond distances in $Mn_{1.1}Fe_{0.9}Si_{0.5}P_{0.5}$.

**Table 5**: Summary of interplanar and intraplanar metal-metal bond distances for $Mn_{1.1}Fe_{0.9}Si_{0.5}P_{0.5}$ across the transition temperature.

| Magnetic State | Intraplanar Mn-Mn (Å) | Intraplanar Fe-Fe (Å) | Interplanar Fe-Mn #1 (Å) | Interplanar Fe-Mn #2 (Å) |
|---|---|---|---|---|
| FM (363K) | 3.259(3) | 2.745(2) | 2.683(3) | 2.749(1) |
| PM (383 K) | 3.205(3) | 2.683(1) | 2.686(3) | 2.769(1) |
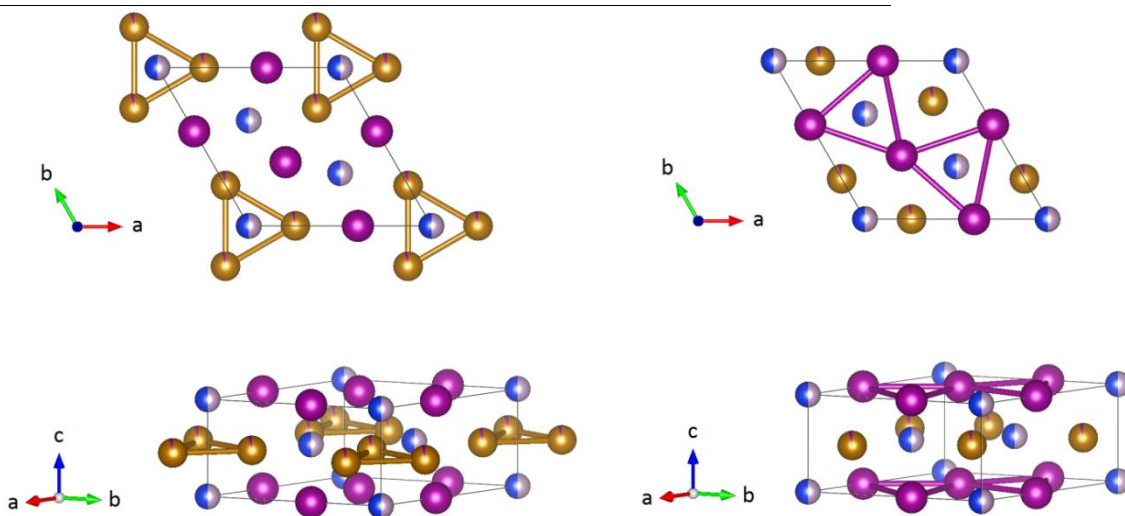


**Figure 20**: Visualization of intraplanar Fe-Fe bonds (left) and Mn-Mn bonds (right) in $Mn_{1.1}Fe_{0.9}Si_{0.5}P_{0.5}$. Mn atoms are violet, Fe atoms are gold, and the Si/P atoms are blue/gray.
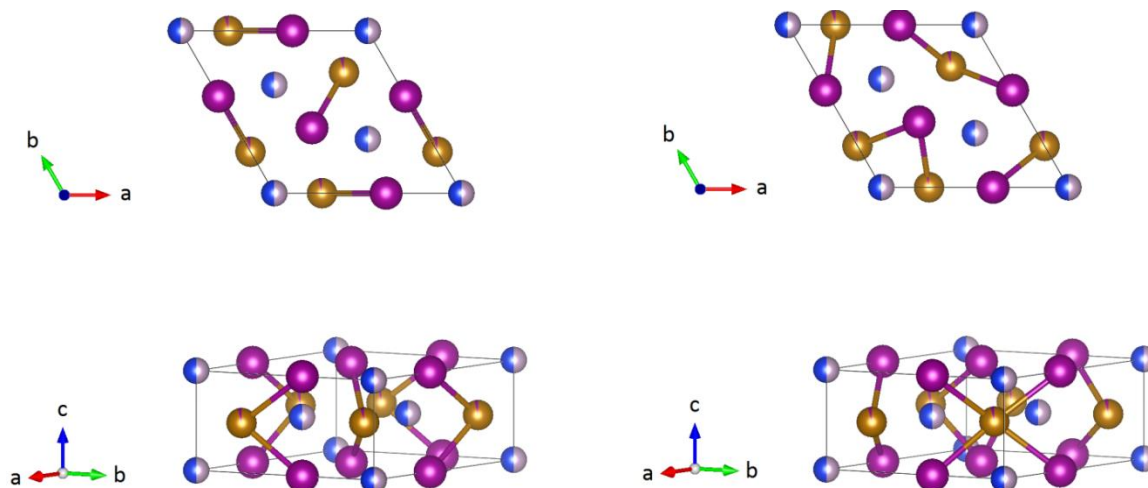


**Figure 21**: Visualization of interplanar Fe-Mn bond #1 (left) and Fe-Mn bond #2 (right) in $Mn_{1.1}Fe_{0.9}Si_{0.5}P_{0.5}$. Mn atoms are violet, Fe atoms are gold, and the Si/P atoms are blue/gray.

*Magnetic Properties*

All samples show sharp paramagnetic-to-ferromagnetic transitions in the magnetization data. Excluding $Mn_{1.4}Fe_{0.6}Si_{0.5}P_{0.5}$, thermal hysteresis is present in all samples (**Figure 22**), which is a signature of a first-order phase transition. Magnetic properties of the series are summarized in **Table 6**. Curie temperatures were taken as the average value between the points of greatest magnetization change during heating and cooling. The magnetic behaviour of $Mn_{2-x}Fe_xSi_{0.5}P_{0.5}$ clearly depends on the Mn content. Firstly, the Curie temperature decreases as Mn amount increases. Secondly, the thermal hysteresis decreases as the samples become Mn richer; a modest hysteresis of 6 K is observed for x = 0.9 and it decreases gradually for larger Mn concentrations and virtually disappears for x = 0.6.

**Table 6**: Summary of magnetic properties for $Mn_{2-x}Fe_xSi_{0.5}P_{0.5}$.

| Composition | $T_c$ (K) | $-\Delta S_m(JKg^{-1}K^{-1})$ (0-2T) | $-\Delta S_m(JKg^{-1}K^{-1})$ (0-5T) | Thermal Hysteresis (K) | Sample mass (mg) |
|---|---|---|---|---|---|
| $Mn_{1.1}Fe_{0.9}Si_{0.5}P_{0.5}$ | 370 | 23.0 | 33.5 | 6 | 1.99 |
| $Mn_{1.2}Fe_{0.8}Si_{0.5}P_{0.5}$ | 332 | 20.5 | 28.6 | 3 | 1.31 |
| $Mn_{1.3}Fe_{0.7}Si_{0.5}P_{0.5}$ | 302 | 11.2 | 22.9 | 1 | 1.92 |
| $Mn_{1.4}Fe_{0.6}Si_{0.5}P_{0.5}$ | 267 | 7.61 | 14.5 | - | 2.40 |
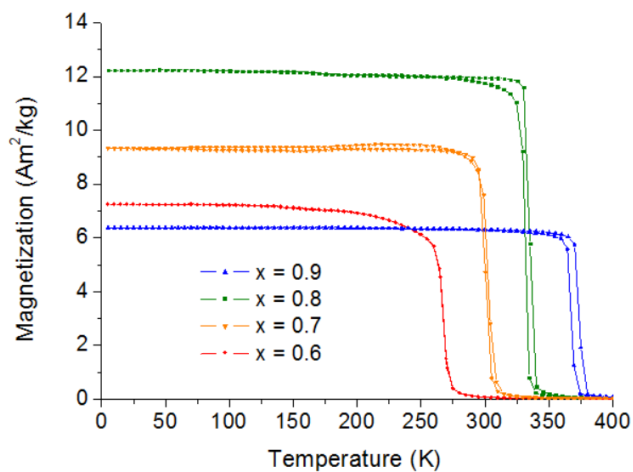
**Figure 22**: Magnetization data for $Mn_{2-x}Fe_xSi_{0.5}P_{0.5}$ in the 100 Oe applied field.
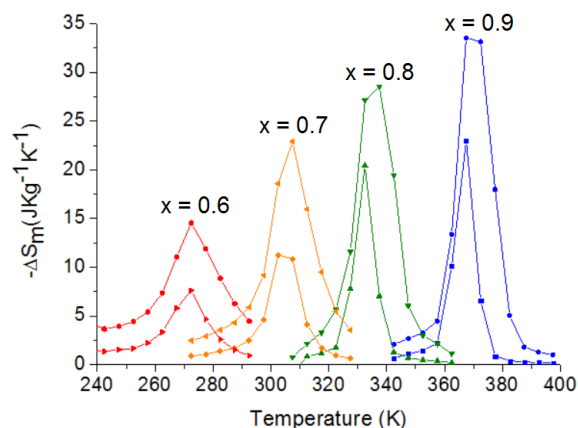


**Figure 23**: Magnetic entropy change for $Mn_{2-x}Fe_xSi_{0.5}P_{0.5}$ as a function of temperature for $\Delta H = 2T$ (lower curves) and 5T (upper curves).

Lastly, with increasing Mn content, the magnitude of magnetic entropy change, -$\Delta S_m$, decreases as the first-order nature of the transition becomes less pronounced (**Figure 23**).  It is worth mentioning that the peak in the magnetic entropy change slightly shifts to higher temperatures with an increased magnetic field for samples x = 0.7, 0.8, and 0.9.  This effect is expected as a larger magnetic field pushes the phase transition to higher temperatures for first-order transitions.[25] For the x = 0.6 sample, the absence of

apparent thermal hysteresis combined with the fact that the $-\Delta S_m$ maximum does not shift to higher temperatures at higher fields might indicate that the phase transition is second-order in nature.  However, the magnitude of magnetic entropy change is about 50% larger than that of the benchmark material, Gd ($-\Delta S_m = -9.8$ JKg$^{-1}$K$^{-1}$ for $\Delta H = 5$T)[7], suggesting that a structural transition is still present. To conclusively establish the nature of the transition, Arrott plots were constructed for x = 0.6 and for x= 0.9 for comparison (**Figure 24**).  The isothermal curves for x = 0.9 have a well-defined S shape above the Curie temperature, indicative of a first-order transition.  The S shape is much less pronounced for x = 0.6 but is still detectable at 275 K, proving that the transition is indeed first order in accordance with the criterion proposed by Banerjee[26].
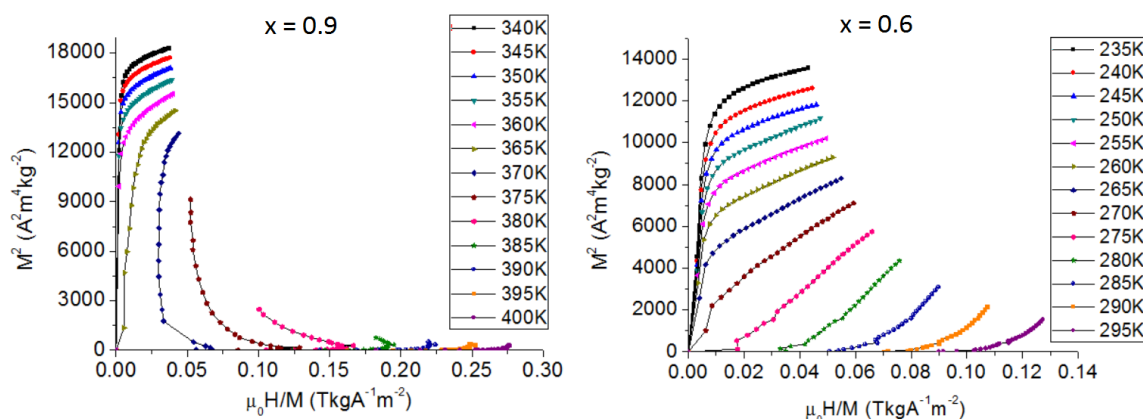


**Figure 24**: Arrott plots derived from magnetic isotherms for x = 0.9 (left), 0.6 (right).

## Conclusions

The Mn$_{2-x}$Fe$_x$Si$_{0.5}$P$_{0.5}$ system is one of the most promising GMCE materials for magnetic cooling.  Desirable properties of this system include the low cost and

abundance of starting materials, easy tunability of both $T_C$ and hysteresis through elemental substitution.   The synthetic method presented in this paper yields pure samples for $0.6 \leq x \leq 0.9$ according to the powder diffraction and magnetization measurements. The results obtained provide more accurate knowledge of the structural and physical properties of the system compared to the previous studies, where secondary phases were present[16,20,21].   The diffraction and magnetization data also suggest that the first-order magnetostructural transition is preserved for the samples with $0.6 \leq x \leq 0.9$. The $Mn_{1.3}Fe_{0.7}Si_{0.5}P_{0.5}$ sample with a $T_C$ close to room temperature and a small thermal hysteresis of 1K is a strong candidate for possible magnetocaloric applications.

**Supporting Information**

Rietveld refinement results for $Mn_{1.1}Fe_{0.9}Si_{0.5}P_{0.5}$ and $Mn_{1.4}Fe_{0.6}Si_{0.5}P_{0.5}$ are presented.
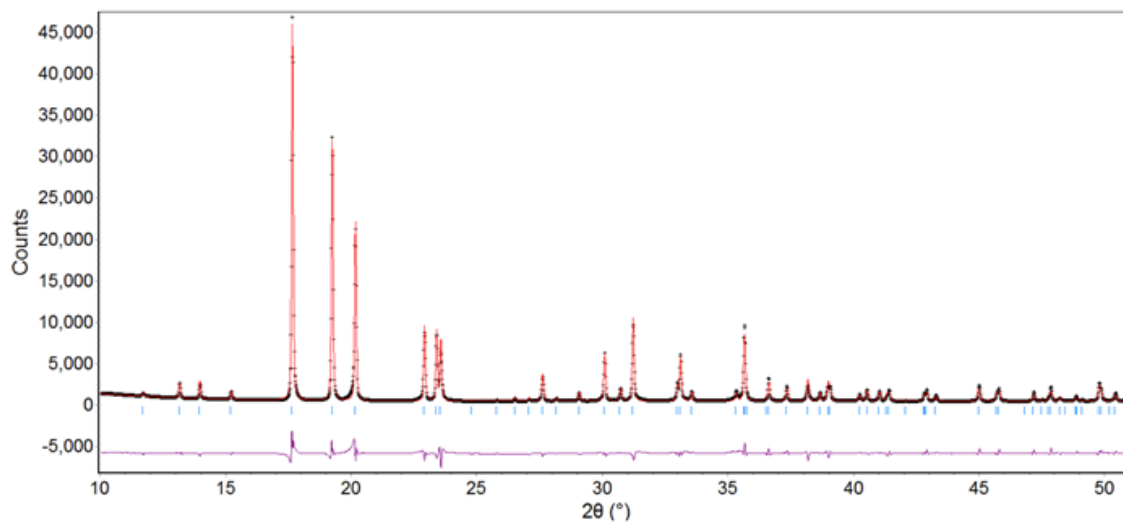


**Figure 1A**: Rietveld refinement of the synchrotron data for $Mn_{1.1}Fe_{0.9}Si_{0.5}P_{0.5}$ at 383 K.
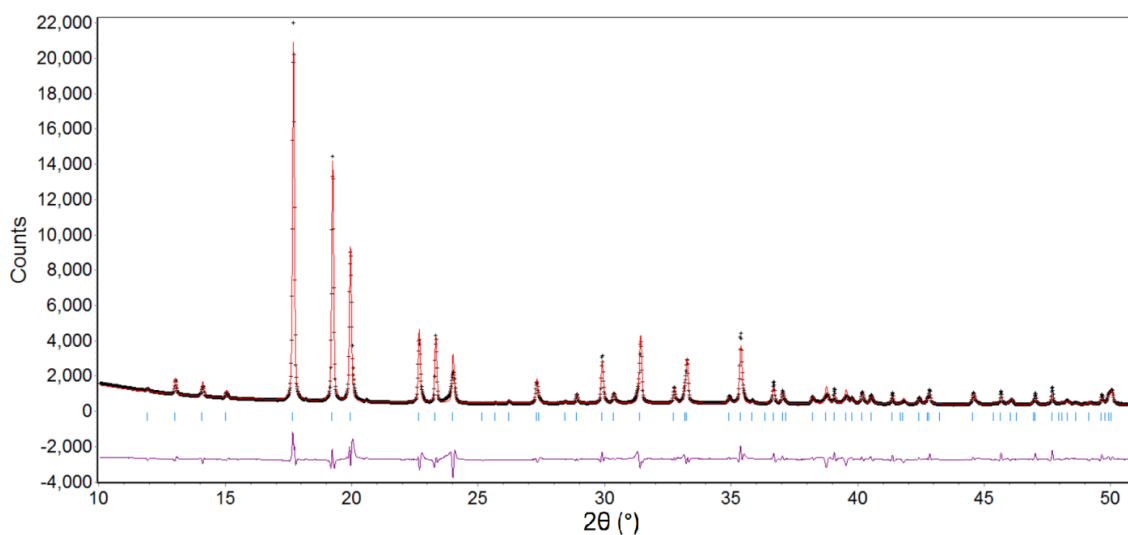


**Figure 2A**: Rietveld refinement of the synchrotron data for $Mn_{1.4}Fe_{0.6}Si_{0.5}P_{0.5}$ at 266 K.
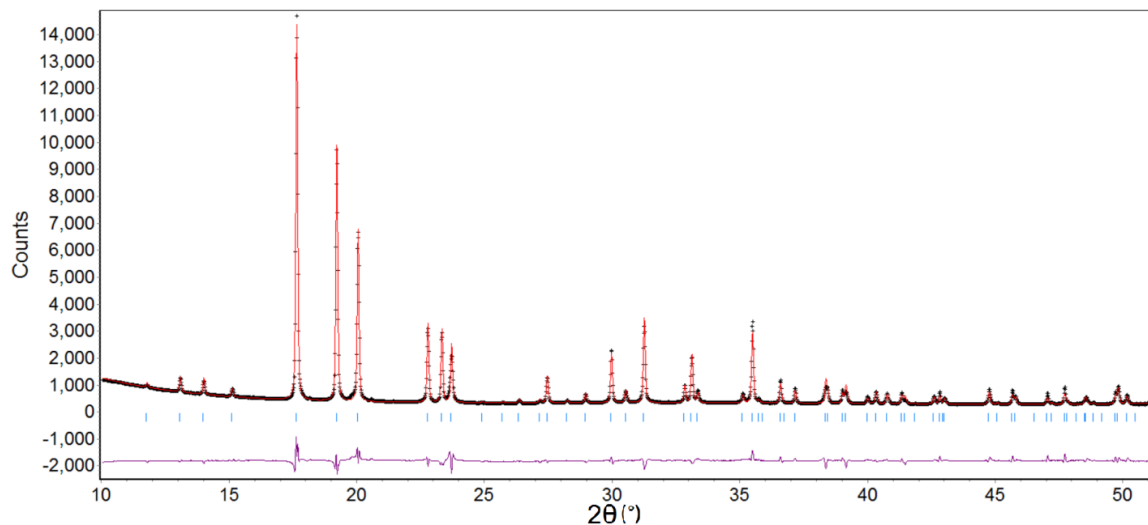
**Figure 3A**: Rietveld refinement of the synchrotron data for $Mn_{1.4}Fe_{0.6}Si_{0.5}P_{0.5}$ at 298 K.

**Table 1A**: Rietveld refinement results for $Mn_{1.1}Fe_{0.9}Si_{0.5}P_{0.5}$ and $Mn_{1.4}Fe_{0.6}Si_{0.5}P_{0.5}$ from the synchrotron data.

| Composition | $Mn_{1.1}Fe_{0.9}Si_{0.5}P_{0.5}$ | | $Mn_{1.4}Fe_{0.6}Si_{0.5}P_{0.5}$ | |
|---|---|---|---|---|
| Temperature (K) | 298 | 383 | 266 | 298 |
| Magnetic state | FM | PM | FM | PM |
| Space group | $P\bar{6}2m$ | $P\bar{6}2m$ | $P\bar{6}2m$ | $P\bar{6}2m$ |
| a/b (Å) | 6.2044(1) | 6.1035(1) | 6.1675(3) | 6.1365(1) |
| c (Å) | 3.2988(1) | 3.4277(1) | 3.3636(2) | 3.4062(1) |
| Volume (Å$^3$) | 109.974(5) | 110.584(5) | 110.810(8) | 111.080(5) |
| Z | 3 | 3 | 3 | 3 |
| 2θ | 10° - 51° | 10° - 51° | 10° - 51° | 10° - 51° |
| Wavelength (Å) | 0.6999 | 0.6999 | 0.6999 | 0.6999 |
| $R_p = \dfrac{\sum_{i=1}^{n}\left|Y_i^{obs} - Y_i^{calc}\right|}{\sum_{i=1}^{n}\left|Y_i^{obs}\right|}$ | 0.063 | 0.067 | 0.069 | 0.046 |
| $R_{wp} = \sqrt{\dfrac{\sum_{i=1}^{n} w_i(Y_i^{obs} - Y_i^{calc})^2}{\sum_{i=1}^{n} w_i(Y_i^{obs})^2}}$ | 0.085 | 0.099 | 0.101 | 0.067 |
| $\chi^2$ | 7.83 | 10.63 | 8.34 | 2.63 |

**Table 2A**: Atomic and isotropic thermal ($B_{iso}$, $Å^2$) parameters $Mn_{1.1}Fe_{0.9}Si_{0.5}P_{0.5}$ and $Mn_{1.4}Fe_{0.6}Si_{0.5}P_{0.5}$.

| Atom | Site | Occup. | x/a | y/b | z/c | $B_{iso}$, $Å^2$ |
|------|------|--------|-----|-----|-----|--------|
| | | | $Mn_{1.1}Fe_{0.9}Si_{0.5}P_{0.5}$, 298K | | | |
| Mn1 | 3f | 1 | 0.5971(2) | 0 | 0 | 0.07(1) |
| Mn/Fe2 | 3g | 0.1/0.9 | 0.2576(2) | 0 | ½ | 0.07(1) |
| Si/P1 | 2d | 0.5/0.5 | 1/3 | 2/3 | ½ | 0.07(1) |
| Si/P2 | 1a | 0.5/0.5 | 0 | 0 | 0 | 0.07(1) |
| | | | $Mn_{1.1}Fe_{0.9}Si_{0.5}P_{0.5}$, 383K | | | |
| Mn1 | 3f | 1 | 0.5926(2) | 0 | 0 | 0.34(2) |
| Mn/Fe2 | 3g | 0.1/0.9 | 0.2538(2) | 0 | ½ | 0.34(2) |
| Si/P1 | 2d | 0.5/0.5 | 1/3 | 2/3 | ½ | 0.34(2) |
| Si/P2 | 1a | 0.5/0.5 | 0 | 0 | 0 | 0.34(2) |
| | | | $Mn_{1.4}Fe_{0.6}Si_{0.5}P_{0.5}$, 266K | | | |
| Mn1 | 3f | 1 | 0.5959(4) | 0 | 0 | 0.17(3) |
| Mn/Fe2 | 3g | 0.4/0.6 | 0.2551(3) | 0 | ½ | 0.17(3) |
| Si/P1 | 2d | 0.5/0.5 | 1/3 | 2/3 | ½ | 0.17(3) |
| Si/P2 | 1a | 0.5/0.5 | 0 | 0 | 0 | 0.17(3) |
| | | | $Mn_{1.4}Fe_{0.6}Si_{0.5}P_{0.5}$, 298K | | | |
| Mn1 | 3f | 1 | 0.5944(3) | 0 | 0 | 0.41(2) |
| Mn/Fe2 | 3g | 0.4/0.6 | 0.2544(2) | 0 | ½ | 0.41(2) |
| Si/P1 | 2d | 0.5/0.5 | 1/3 | 2/3 | ½ | 0.41(2) |
| Si/P2 | 1a | 0.5/0.5 | 0 | 0 | 0 | 0.41(2) |

## **Acknowledgements**

## References

(1) Thomson, William. *Cyclopedia of the Physical Sciences*, 2nd ed.; J.P. Nichol (ed.). Richard Green and Company, London and Glasgow, **1860**.

(2) Thomson, William. II. On the Thermoelastic, Thermomagnetic, and Pyroelectric Properties of Matter. *Phil. Mag*. *Ser. 5*. **1878**, *5*, 4 – 27.

(3) Weiss, P.; Piccard, A. A new magnetic thermal phenomenon. *C. R. Acad. Sci*. **1918**, *166*, 352.

(4) Shirron, P. J.; Kimball, M. O.; James, B. L.; Muench, T.; DiPirro, M. J.; Bialas, T. G.; Sneiderman, G. A.; Porter, F. S.; Kelley, R. L. Thermodynamic performance of the 3-stage ADR for the Astro-H Soft-X-ray Spectrometer instrument. *Cryogenics*. **2016**, *74*, 24 – 30.

(5) Giauque, W.F.; MacDougall, D.P. Attainment of Temperatures Below 1° Absolute by Demagnetization of $Gd_2(SO_4)_3 \cdot 8H_2O$. *Phys. Rev.* **1933**, *43*, 768.

(6) Brown, G. V. Magnetic heat pumping near room temperature. *J. Appl. Phys.* **1976**, *47*, 3673 – 3680.

(7) Pecharsky, V. K.; Gschneidner, K. A., Jr. Giant Magnetocaloric Effect in $Gd_5(Si_2Ge_2)$. *Phys. Rev. Lett.* **1997**, *78*, 4494 – 4497.

(8) Pecharsky, V. K.; Gschneidner, K. A., Jr. Magnetocaloric effect associated with magnetostructural transitions. *Springer Series in Materials Science*. **2005**, *79*, 199 – 222.

(9) Hu, F. X.; Shen, B. G.; Sun, J. R.; Cheng, Z. H.; Rao, G. H.; Zhang, X. X. Influence of negative lattice expansion and metamagnetic transition on magnetic entropy change in the compound $LaFe_{11.4}Si_{1.6}$. *Appl. Phys. Lett*. **2001**, *78*, 3675 – 3677.

(10) Hu, F. X., Shen, B. G., Sun, J. R., Wang, G. J.; Cheng, Z. H. Very large magnetic entropy change near room temperature in $LaFe_{11.2}Co_{0.7}Si_{1.1}$. *Appl. Phys. Lett.* **2002**, *80*, 826 – 828.

(11) Wada, H.; Tanabe, Y. Giant magnetocaloric effect of $MnAs_{1-x}Sb_x$. *Appl. Phys. Lett.* **2001**, *79*, 3302 – 3304.

(12) Wada, H.; Morikawa, T.; Taniguchi, K.; Shibata, T.; Yamada, Y.; Akishige, Y. Giant magnetocaloric effect of $MnAs_{1-x}Sb_x$ in the vicinity of first-order magnetic transition. *Physica B*. **2003**, *328*, 114 – 116.

(13) Tegus, O.; Brück, E.; Buschow, K. H. J.; de Boer, F. R. Transition-metal-based magnetic refrigerants for room-temperature applications. *Nature*. **2002**, *415*, 150 – 152.

(14) Brück, E.; Ilyn, M.; Tishin, A. M.; Tegus, O. Magnetocaloric effects in $MnFeP_{1-x}As_x$-based compounds. *J. Magn. Magn. Mater*. **2005**, *290 – 291*, 8 – 13.

(15) Thanh, D. T. C.; Brück, E.; Tegus, O.; Klaasse, J. C. P.; Gortenmulder, T. J.; Buschow, K. H. J. Magnetocaloric effect in MnFe(P,Si,Ge) compounds. *J. Appl. Phys*. **2006**, *99*, 08Q107-1 – 08Q107-3.

(16) Thanh, D. T. C.; Brück, E.; Trung, N. T.; Klaasse, J. C. P.; Buschow, K. H. J.; Ou, Z. Q.; Tegus, O.; Caron, L.

Structure, magnetism, and magnetocaloric properties of $MnFeP_{1-x}Si_x$. *J. Appl. Phys.* **2008**, *103*, 07B318-1 – 07B318-3.

(17) Höglin, V.; Hudl, M.; Sahlberg, M.; Nordblad, P.; Beran, P.; Andersson, Y. The crystal and magnetic structure of the magnetocaloric compound $FeMnP_{0.5}Si_{0.5}$. *J. Solid State Chemistry*. **2011**, *184*, 2434 – 2438.

(18) Tegus, O.; Li-Hong B.; Lin, S. Phase transitions and magnetocaloric effects in intermetallic compounds MnFeX (X=P, As, Si, Ge). *Chin. Phys. B.* **2013**, *22*, 037506-1 – 037506-9.

(19) Yibole, H.; Guillou, F.; Zhang, L.; van Dijk, N. H.; Brück, E. Direct measurement of the magnetocaloric effect in MnFe(P,X) (X = As, Ge, Si) materials. *Journal of Physics D: Applied Physics*. **2014**, *47*, 075002-1 – 075002-9.

(20) Dung, N. H.; Zhang, L.; Ou, Z. Q.; Brück, E. From first-order magneto-elastic to magneto-structural transition in $(Mn,Fe)_{1.95}P_{0.50}Si_{0.50}$ compounds. *Appl. Phys. Lett.* **2011**, *99*, 092511-1 – 092511-3.

(21) Dung, N. H.; Zhang, L.; Ou, Z. Q.; Zhao, L.; van Eijck, L.; Mulders, A. M.; Avdeev, M.; Suard, E.; van Dijk, N. H.; Brück, E. High/low-moment phase transition in hexagonal Mn-Fe-P-Si compounds. *Phys. Rev. B*. **2012**, *86*, 045134-1 – 045134-7.

(22) B. Carlsson, M. Gölin, S. Rundqvist. Determination of the Homogeneity Range and Refinement of the Crystal Structure of $Fe_2P$. *J. Solid State Chem.* **1973**, *8*, 57 – 67.

(23) Höglin, V.; Hudl, M.; Caron, L.; Beran, P.; Sørby, M. H.; Nordblad, P.; Andersson, Y.; Sahlberg, M. Detailed study of the magnetic ordering in $FeMnP_{0.75}Si_{0.25}$. *J. Solid State Chem*. **2015**, *221*, 240 – 246.

(24) Hunter, B. A.; Howard, C. J. Rietica; Australian Nuclear Science and Technology Organization: Menai, Australia, **2000**.

(25) Tishin, A. M.; Spichkin, Y. I. *The Magnetocaloric Effect and its Applications.* Institute of Physics Publishing: Bristol and Philadelphia, **2003**.

(26) Banerjee, S. K. On a Generalised Approach to First and Second Order Magnetic Transitions. *Phys. Lett.* **1964**, *12*, 16 – 17.

## Chapter 6. Structural and Magnetic Properties of the Magnetocaloric MnFe(Si,P) Phases

### Abstract

The MnFeSi$_x$P$_{1-x}$ phases (x = 0.30, 0.35, 0.40, 0.48, 0.52, 0.54, 0.56) have been synthesized by arc-melting and subsequent high temperature sintering. For the first time, single crystals of x = 0.30, 0.40 were successfully grown and analyzed by single crystal x-ray diffraction. Variable temperature x-ray diffraction experiments for x = 0.30 were completed which show the structural changes across the phase transition. Magnetization data revealed that the Curie temperatures and thermal hysteresis values can be tuned according to the Si:P ratio.

### Introduction

The initiative toward renewable, green energy has led to the pursuit of magnetic cooling through the use of magnetocaloric materials. These materials are able to convert their internal magnetic energy (magnetic entropy) into thermal energy (phonon excitations) in a reversible process called the magnetocaloric effect (MCE). The field of MCE materials became a subject of intense study after the discovery of the Gd$_5$(Si,Ge)$_4$ phases[1]. Pecharsky and Gschneidner found that as the material went from ferromagnetic to paramagnetic, a simultaneous first-order change in the crystal lattice is induced by the reorientation of magnetic moments. This structural transition boosted the magnetocaloric response of the material immensely and the resulting effect is called

giant MCE (GMCE). The $Gd_5(Si,Ge)_4$ phases exhibit what is known as a first-order magnetic phase transition. The presence of the structural change that accompanies the magnetic phase transition has been found to be one of the key factors in obtaining a GMCE. To be of any use in commercial applications, a large MCE should be obtained with magnetic fields of modest size provided by permanent magnets (1-2T). Currently, some of the leading systems that possess the largest known magnetic entropy change include: $RE_5(Si,Ge)_4$-based[2-4], MnAs-based[5-7], $LaFe_{13-x}Si_x$-based[8,9], and $Fe_2P$-based[10-12], systems. The discovery of new magnetocaloric phases with first-order phase transitions and large MCE is necessary to push these materials in the direction of commercialization. The reasons to go toward magnetic cooling are plentiful.

Studies have shown that magnetic cooling systems can offer a Carnot efficiency of around 60% compared to the 40% Carnot efficiency of vapour compression technology, a substantial increase in cooling efficiency[13-15]. In addition to being more efficient, magnetocaloric materials are also more environmentally friendly since they do not require the use of known ozone-depleting chemicals (i.e. chlorofluorocarbons) found in vapour-based systems. In terms of cost, the fabrication of $(Mn,Fe)_2(Si,P)$ magnetocaloric materials includes very abundant elements, making the cost very affordable. Toxic elements are also avoided in the composition making the environmental benefits even greater. Furthermore, since we are dealing with solid materials, more compact cooling units can be made compared to their vapour

counterparts which need ample space for gas compression.  It is possible to synthesize a material that is more efficient than the best commercial cooling systems while being environmentally friendly and cheap.

One of the major problems facing the $Fe_2P$-based system is the degree of thermal hysteresis.  In systems with small hysteresis, the entropy change is localized near $T_c$ for a targeted operational temperature range.  In the case of large hysteresis, the magnetic entropy change is diluted over the whole range making it less effective for cooling applications.  Previously, we have shown that $T_c$, hysteresis, and magnetic entropy change can be carefully tuned by changing the Mn:Fe content of the material[16].  Herein, we report the changes associated by changing the Si:P content while keeping the metal:metal content constant for the $MnFeSi_xP_{1-x}$ system.   As the phases become more silicon deficient, there is a drop in the Curie temperature along with enlarged thermal hysteresis.  On the silicon-rich side, the Curie temperature increases to a maximum at x = 0.52 and falls for additional Si content.  There is no observable change in the thermal hysteresis for the silicon-rich samples.  For the first time, single crystals of these silicon deficient phases were analyzed and characterized through x-ray diffraction. Temperature dependent experiments on a single crystal of x = 0.30 were completed from 90K – 294K which provide a complete structural description of the first order phase transition across the Curie temperature.

**Experimental**

*Synthesis of MnFeSi$_x$P$_{1-x}$*

Prior to arc-melting, the brown oxide layer on the Mn pieces was removed using dilute nitric acid (5-10 wt.%).  Pieces of Mn (99.9 wt.%, Alfa Aesar), lumps of Si (99.999 wt.%, Alfa Aesar) and Fe granules (99.98 wt.%, Alfa Aesar) were brought into the welding chamber, loaded on a water-cooled copper hearth, flushed with Ar gas (>99.999%) and were arc-melted using a tungsten electrode.  The buttons were flipped and remelted several times to improve homogeneity and were within 1% error of the theoretical yield. The resultant ingot was taken into the glovebox (Ar atmosphere, <0.1 O$_2$ ppm, <0.1 H$_2$O ppm) where it was ground into a fine powder before mixing thoroughly with red P (99.5 wt.% CERAC Specialty Inorganics),  pressed into 10 mm diameter pellets and subsequently sealed in evacuated silica tubes. To counteract the high vapour pressure of red P, the samples were first heated to 270°C at 50°C/h and sustained for 12h.  They were then heated up to 1050°C at 100°C/h, annealed for 1 week and quenched in cold water.  It is necessary to introduce a second annealing for the sintered samples which were reground, repressed, sealed in evacuated silica tubes, heated to 1050°C at 100°C/h and annealed for 1 week.   After the second annealing, they were slowly cooled to 400°C and finally quenched in cold water.

*Powder X-ray Diffraction (PXRD) and Single Crystal X-ray Diffraction Studies*

PXRD data were collected from $2\theta$ = 20°-70° on a PANalytical X'Pert Pro diffractometer with a linear X'Celerator detector using $CuK\alpha_1$ radiation at room temperature. Phase analyses of the polycrystalline samples and Rietveld refinement of the lattice parameters were performed using the Rietica software[17].

Single crystal diffraction studies were done for the sample of x = 0.30, 0.40 to characterize the structural change across the phase transition. Variable temperature experiments were completed for the sample of x = 0.30 and was cooled with liquid nitrogen at a rate of 5K/min. Unit cell indexing was completed by collecting 48 frames, in 5K intervals, for temperatures close to $T_c$ and the interval was increased up to 25K for temperatures far from the transition point. The data was collected on a Bruker APEX II X-ray diffractometer using a CCD detector with $MoK\alpha$ radiation. Full data sets were collected at 90K and at room temperature for structural solutions using SHELXL software.[18]

*Magnetic Property Measurements*

Mass magnetization data were collected for x = 0.30, 0.35, 0.40, 0.48, 0.52, 0.54, 0.56 on a Quantum Design SQUID MPMS magnetometer between 5 and 400K with steps of 5K and applied field of 100 Oe. Thermal hysteresis loops were measured for each sample where the magnetization was measured on cooling and subsequently on

heating. The ramping and cooling rate for all magnetization measurements were done at 10K/min and sufficient time was allowed for the sample to equilibrate at the target temperature before a reading was taken.

## Results and Discussion

*Structural Parameters and Phase Transition*

The lattice parameters and volume for the unit cell of $MnFeSi_xP_{1-x}$ (x = 0.3, 0.35, 0.4, 0.48, 0.52, 0.54, 0.56) are shown below in **Table 7**. Rietveld refinement of powder x-ray diffraction data revealed the polycrystalline samples adopt a hexagonal type symmetry with a $P\bar{6}2m$ space group. A representative diffraction pattern is shown in **Figure 25**, where the Bragg peaks associated with the $Fe_2P$-type phase are indicated below the spectra.
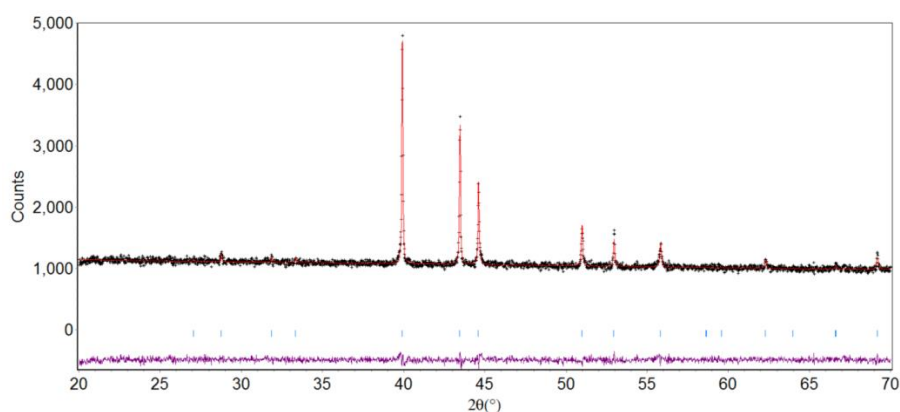


**Figure 25**: Rietveld refinement of the powder x-ray diffraction pattern for $MnFeSi_{0.48}P_{0.52}$ using $\lambda$ = 1.5406Å.

**Table 7**: Unit cell parameters for $MnFeSi_xP_{1-x}$ collected at 298K.

| Composition | a/b (Å) | c (Å) | Vol. (Å$^3$) |
|---|---|---|---|
| $MnFeSi_{0.30}P_{0.70}$ (x = 0.30) | 5.9970(3) | 3.4927(2) | 108.78(1) |
| $MnFeSi_{0.35}P_{0.65}$ (x = 0.35) | 6.0120(3) | 3.4873(2) | 109.16(1) |
| $MnFeSi_{0.40}P_{0.60}$ (x = 0.40) | 6.0296(5) | 3.4792(2) | 109.54(1) |
| $MnFeSi_{0.40}P_{0.60}$ (x = 0.40) | 6.1818(4) | 3.3110(3) | 109.58(1) |
| $MnFeSi_{0.48}P_{0.52}$ (x = 0.48) | 6.2011(4) | 3.2915(3) | 109.62(1) |
| $MnFeSi_{0.52}P_{0.48}$ (x = 0.52) | 6.2084(3) | 3.2856(2) | 109.68(1) |
| $MnFeSi_{0.54}P_{0.46}$ (x = 0.54) | 6.2084(3) | 3.2877(2) | 109.74(1) |
| $MnFeSi_{0.56}P_{0.44}$ (x = 0.56) | 6.2065(2) | 3.2877(1) | 109.68(1) |

For the silicon deficient samples (x = 0.30, 0.35, 0.40, 0.48), the lattice constants *a* and *c* monotonically increase and decrease respectively with additional Si content (see **Figure 26**).  There is a steady increase in unit cell volume as a result of the larger atomic radius of Si compared to P.  When the phase becomes silicon rich (x > 0.50), there starts to become indication of a secondary phase, $(Mn,Fe)_3Si$, and the unit cell trend becomes unclear.  Ideally, if the main phase were to accept all of the incoming silicon, the trend should proceed as before however since the secondary phase can take out varying amounts of Mn, Fe, and Si, we ultimately see a decrease in the unit cell volume.  This supports the findings of Hoglin et al.[19] who claim a 3 phase region for x > 0.50 composed of the $Fe_2P$-type phase, $(Mn,Fe)_3Si$, and $(Mn,Fe)_5Si_3$.
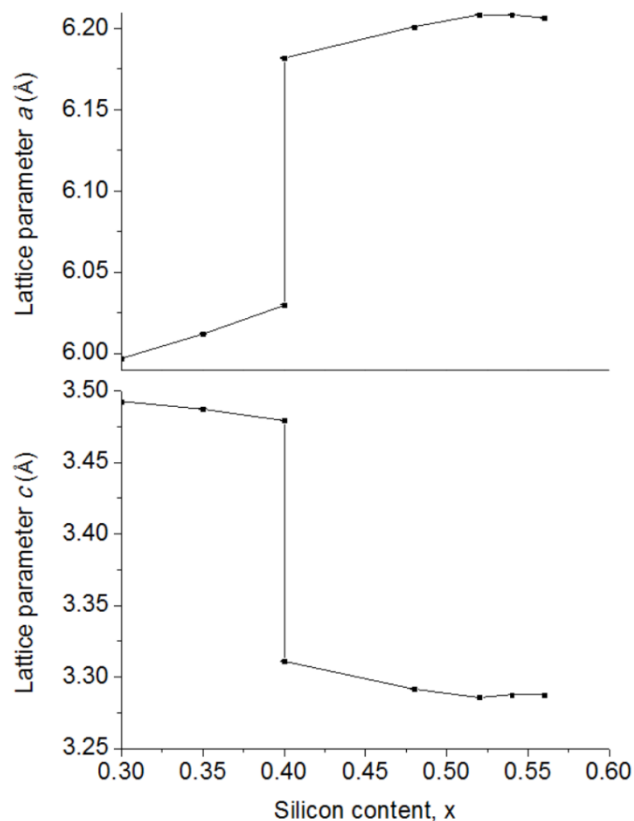
**Figure 26**: Lattice parameters $a$ and c as a function of silicon content. The error bars are smaller than the data points.

All of the Si deficient phases (x < 0.50) are single phase according to the powder x-ray diffraction data. It should be noted that the composition, $MnFeSi_{0.40}P_{0.60}$, is observed to have two unit cells of the $Fe_2P$-type phase at room temperature. This is due to the structural transition which occurs at room temperature for this composition.

The structural change across the Curie temperature for the silicon deficient phases is much larger compared to the change seen in the $Mn_{2-x}Fe_xSi_{0.5}P_{0.5}$ phases[16]. To study this more closely, single crystal x-ray diffraction experiments were done for x = 0.30, 0.40. Small single crystals were obtained for these samples after the reannealing

process at 1050°C.  Upon cooling, variable temperature scans for x = 0.30 (approximately 0.12 mm x 0.08 mm x 0.03 mm in size) revealed a transition temperature of $T_t$ = 137.5K that involves a discontinuous increase and decrease in lattice parameters *a* and *c* respectively (see **Figure 27**).   Upon heating, the lattice parameters discontinuously change in the opposite direction ($T_t$ = 237.5K). These transition temperatures obtained are very close to the Curie temperatures obtained upon heating and cooling (see **Figure 28**), and the small discrepancy may be due to differences in ramping rate.  This is very strong evidence of a first-order phase transition.  The refinement results and details of the experiment are summarized in **Table 8** for $MnFeSi_{0.3}P_{0.7}$ at 90K and 294K which have $R_1$ values of 0.0583 and 0.0211 respectively.



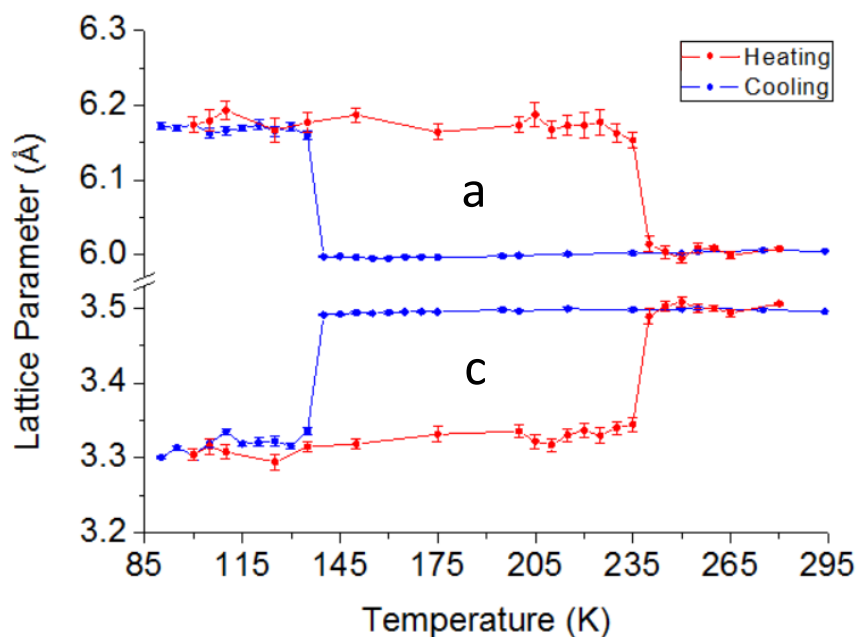**Figure 27**: Variable temperature single crystal x-ray diffraction experiment for $MnFeSi_{0.3}P_{0.7}$ from 90 K – 294 K.

Table 8: Refinement results for the single crystal of $MnFeSi_{0.3}P_{0.7}$.

| Phase | $MnFeSi_{0.3}P_{0.7}$ | $MnFeSi_{0.3}P_{0.7}$ |
|---|---|---|
| Temperature | 90K | 294K |
| Space Group | $P\bar{6}2m$ | $P\bar{6}2m$ |
| Lattice parameters (Å) | a = 6.1721(9) | a = 6.0043(2) |
| | b = 6.1721(9) | b = 6.0043(2) |
| | c = 3.3006(7) | c = 3.4954(1) |
| Volume ($Å^3$) | 108.89(4) | 109.13(1) |
| Z | 3 | 3 |
| Θ-Range for data collection | 3.812 to 45.375° | 3.919 to 45.253° |
| Index range | $-10 \le h \le 12$ | $-11 \le h \le 11$ |
| | $-12 \le k \le 11$ | $-11 \le k \le 11$ |
| | $-6 \le l \le 6$ | $-6 \le l \le 6$ |
| Reflections collected | 3633 | 3627 |
| Independent reflections | 376 [R(int) = 0.1728] | 368 [R(int) = 0.0513] |
| Completeness to max 2Θ | 98.2 | 100 |
| Data/restraints/parameters | 376/0/14 | 368/0/14 |
| Goodness-of-fit on $F^2$ | 0.963 | 1.193 |
| Final R indices [I>2σ(I)] | R1 = 0.0436, wR2 = 0.0887 | R1 = 0.0203, wR2 = 0.0598 |
| R indices (all data) | R1 = 0.0583, wR2 = 0.0913 | R1 = 0.0211, wR2 = 0.0601 |
| Largest diff. peak/hole ($e^-/ Å^3$) | 1.763/-2.165 | 1.032/-1.105 |

The metal atoms were found to occupy the 3f and 3g sites and the atomic parameters for the unit cell are presented below in **Table 9**.  Due to the similar atomic scattering factors of Mn and Fe as well as Si and P, the occupancies for the sites could not be refined and their distribution were assumed to be consistent with the sample composition (i.e. 50/50 distribution of Mn and Fe on the 3f and 3g sites, 30/70 distribution of Si and P on the 2d and 1a sites).  The first-order phase transition of this material indicate that the magnetic moments of Mn and Fe are directly linked to the

atomic structure and therefore the position of the metal sites are expected to change whether it is paramagnetic or ferromagnetic. Refinement of the fractional coordinate, x, for the two metal sites (3f and 3g) showed a dramatic increase as the temperature is lowered.

**Table 9**: Refined atomic parameters for $MnFeSi_{0.3}P_{0.7}$ at 90K and 294K.

| Atom | Site | Occupancy | x | y | z | $U_{eq}$ ($Å^3$) |
|------|------|-----------|---|---|---|------------------|
| **$MnFeSi_{0.3}P_{0.7}$ (90K)** | | | | | | |
| **Mn1/Fe1** | 3f | 0.5/0.5[a] | 0.5965(3) | 0 | 0 | 0.0076(3) |
| **Mn2/Fe2** | 3g | 0.5/0.5[a] | 0.2572(3) | 0 | 1/2 | 0.0064(3) |
| **Si1/P1** | 2d | 0.3/0.7[a] | 1/3 | 2/3 | 1/2 | 0.0067(7) |
| **Si2/P2** | 1a | 0.3/0.7[a] | 0 | 0 | 0 | 0.0062(5) |
| | | | | | | |
| **$MnFeSi_{0.3}P_{0.7}$ (294K)** | | | | | | |
| **Mn1/Fe1** | 3f | 0.5/0.5[a] | 0.5896(2) | 0 | 0 | 0.0081(2) |
| **Mn2/Fe2** | 3g | 0.5/0.5[a] | 0.2537(1) | 0 | 1/2 | 0.0069(1) |
| **Si1/P1** | 2d | 0.3/0.7[a] | 1/3 | 2/3 | 1/2 | 0.0079(4) |
| **Si2/P2** | 1a | 0.3/0.7[a] | 0 | 0 | 0 | 0.0062(2) |

[a]All occupancies were fixed

*Magnetic Properties*

For the sake of clarity, the magnetization data for the silicon deficient phases (see **Figure 28**) are shown separately from the silicon rich phases (**Figure 29**).
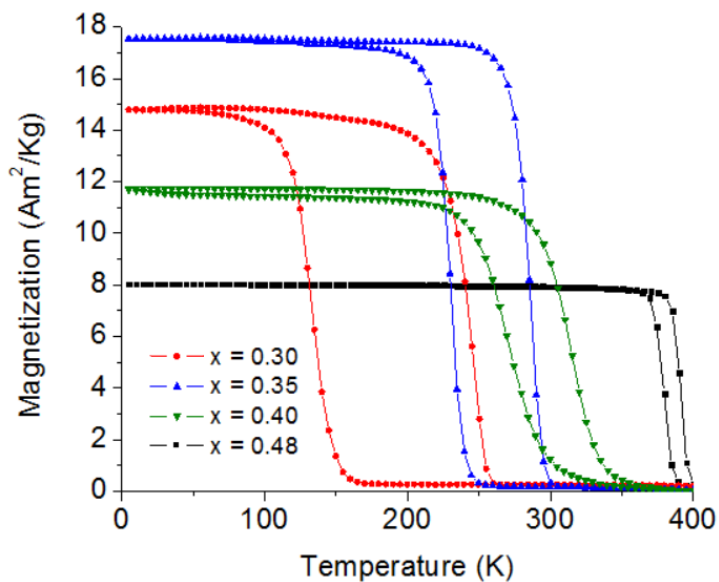
**Figure 28**: Magnetization curves for the silicon deficient phases $MnFeSi_xP_{1-x}$, x < 0.50.
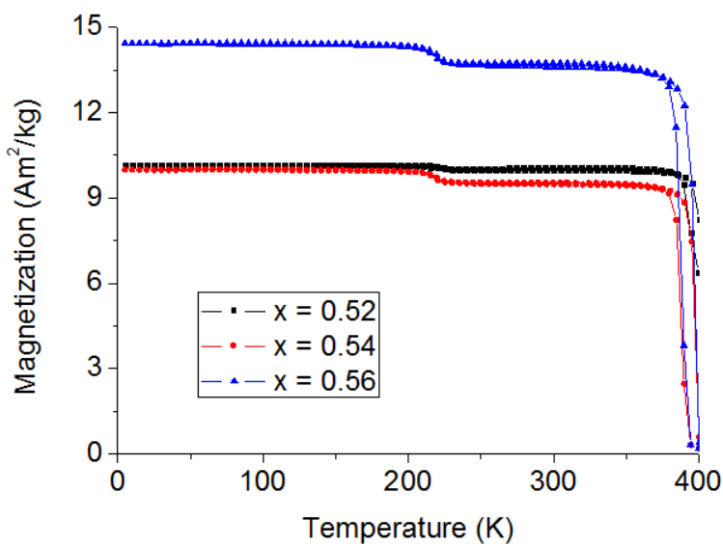


**Figure 29**: Magnetization curves for the silicon rich phases $MnFeSi_xP_{1-x}$, x > 0.50.

**Table 10**: Magnetic properties for the Si rich and Si deficient phases.

| Composition | $T_c$ (K) | Thermal Hysteresis (K) |
|---|---|---|
| $MnFeSi_{0.30}P_{0.70}$ | 193 | 110 |
| $MnFeSi_{0.35}P_{0.65}$ | 260 | 56 |
| $MnFeSi_{0.40}P_{0.60}$ | 292 | 41 |
| $MnFeSi_{0.48}P_{0.52}$ | 388 | 11 |
| $MnFeSi_{0.52}P_{0.48}$ | >400 | - |
| $MnFeSi_{0.54}P_{0.46}$ | 393 | 11 |
| $MnFeSi_{0.56}P_{0.44}$ | 392 | 11 |

All of the samples shown have a sharp paramagnetic to ferromagnetic transition upon heating to a sufficient temperature.  Silicon content is observed to have a direct correlation with the degree of thermal hysteresis and $T_c$.  For an increase in silicon content, the thermal hysteresis can be tuned from a gigantic 110K for x = 0.3 to around 11K for x = 0.48.  Accompanying the decrease in hysteresis is an increase in the $T_c$ up until x = 0.52 reaching a temperature of over 400K.  The $T_c$ drops slightly for even higher Si content.  The transition temperature for each sample was calculated by averaging the points of greatest magnetization change in the heating and cooling curves.

## Conclusions

Currently, the $(Mn,Fe)_2(Si,P)$ system is one of the strongest candidates for potential magnetocaloric applications.  It features cheap and rare-earth free, abundant, non-toxic elements along with easy tuning of its magnetic properties.  The structural parameters of silicon deficient/rich phases of the system $MnFeSi_xP_{1-x}$ were characterized through powder x-ray diffraction and variable-temperature single crystal experiments.  This data was complimented with magnetic property measurements for determination of $T_c$ and thermal hysteresis of the samples.  We have found that altering the Si/P ratio of this system allows for direct control of hysteresis and Curie temperature.

**Supporting Information**

Refinement results from a single-crystal experiment (294K) for $MnFeSi_{0.4}P_{0.6}$ are summarized.

**Table 1B**: Refinement results for the single crystal of $MnFeSi_{0.4}P_{0.6}$.

| Phase | $MnFeSi_{0.4}P_{0.6}$ |
|---|---|
| Temperature | 294K |
| Space Group | $P\bar{6}2m$ |
| Lattice parameters (Å) | 6.0214(9) |
| | 6.0214(9) |
| | 3.4689(7) |
| Volume ($Å^3$) | 108.92(4) |
| Z | 3 |
| Θ-Range for data collection | 3.908 to 34.333° |
| Index range | $-8 \le h \le 8$ <br> $-9 \le k \le 9$ <br> $-5 \le l \le 5$ |
| Reflections collected | 1331 |
| Independent reflections | 194 [R(int) = 0.0886] |
| Completeness to max 2Θ | 96.6% |
| Data/restraints/parameters | 194/0/16 |
| Goodness-of-fit on $F^2$ | 1.212 |
| Final R indices [I>2σ(I)] | $R_1 = 0.0405$, $wR_2 = 0.1056$ |
| R indices (all data) | $R_1 = 0.0407$, $wR_2 = 0.1057$ |
| Largest diff. peak/hole ($e^-/Å^3$) | 1.254/-1.114 |

**Table 2B**: Refined atomic parameters for $MnFeSi_{0.4}P_{0.6}$ at 294K.

| Atom | Site | Occupancy | x | y | z | $U_{eq}$ ($Å^3$) |
|------|------|-----------|---|---|---|--------|
| $MnFeSi_{0.40}P_{0.60}$ (294K) | | | | | | |
| Mn1/Fe1 | 3f | 0.5/0.5 | 0.5895(4) | 0 | 0 | 0.0082(7) |
| Mn2/Fe2 | 3g | 0.5/0.5 | 0.2536(3) | 0 | 1/2 | 0.0070(6) |
| Si1/P1 | 2d | 0.4/0.6 | 0 | 0 | 0 | 0.009(1) |
| Si2/P2 | 1a | 0.4/0.6 | 2/3 | 1/3 | 1/2 | 0.0066(8) |

## Acknowledgements

## References

(1) Pecharsky, V. K.; Gschneidner, K. A., Jr. Giant Magnetocaloric Effect in $Gd_5(Si_2Ge_2)$. *Phys. Rev. Lett.* **1997**, *78*, 4494 – 4497.

(2) Gschneidner, K. A., Jr.; Pecharsky, V. K. Magnetocaloric Materials. *Annu. Rev. Mater. Sci.* **2000**, *30*, 387–429.

(3) Spichkin, Y. I.; Pecharsky, V. K.; Gschneidner, K. A. Preparation, crystal structure, magnetic and magnetothermal properties of $(Gd_xR_{5-x})Si_4$, where R=Pr and Tb, alloys. *J. Appl. Phys.* **2001**, *89(3)*, 1738–1745.

(4) Gschneidner, K. A., Jr.; Pecharsky, V. K.; Pecharsky, A. O.; Ivtchenko, V. V.; Levin, E. M. The nonpareil $R_5(Si_xGe_{1-x})_4$ phases. *J. Alloys Compd.* **2000**, *303–304*, 214–222.

(5) Wada, H.; Morikawa, T.; Taniguchi, K.; Shibata, T.; Yamada, Y.; Akishige, Y. Giant magnetocaloric effect of $MnAs_{1-x}Sb_x$ in the vicinity of first-order magnetic transition. *Physica B*. **2003**, *328(1–2)*, 114–116.

(6) Wada, H.; Tanabe, Y. Giant magnetocaloric effect of $MnAs_{1-x}Sb_x$. *Appl. Phys. Lett*. **2001**, *79(20)*, 3302–3304.

(7) Carvalho, A. M. G.; Coelho, A. A.; von Ranke, P. J.; Alves, C. S. The isothermal variation of entropy ($\Delta S_T$) may be miscalculated from magnetization isotherms in some cases: MnAs and $Gd_5Ge_2Si_2$ compounds as examples. *J. Alloys Compd*. **2011**, *509(8)*, 3452–3456.

(8) Hu, F. X.; Shen, B. G.; Sun, J. R.; Cheng, Z. H.; Rao, G. H.; Zhang, X. X. Influence of negative lattice expansion and metamagnetic transition on magnetic entropy change in the compound $LaFe_{11.4}Si_{1.6}$. *Appl. Phys. Lett*. **2001**, *78*, 3675 – 3677.

(9) Hu, F. X., Shen, B. G., Sun, J. R., Wang, G. J.; Cheng, Z. H. Very large magnetic entropy change near room temperature in $LaFe_{11.2}Co_{0.7}Si_{1.1}$. *Appl. Phys. Lett.* **2002**, *80*, 826 – 828.

(10) Tegus, O.; Brück, E.; Buschow, K. H. J.; de Boer, F. R. Transition-metal-based magnetic refrigerants for room-temperature applications. *Nature*. **2002**, *415*, 150 – 152.

(11) Brück, E.; Ilyn, M.; Tishin, A. M.; Tegus, O. Magnetocaloric effects in $MnFeP_{1-x}As_x$-based compounds. *J. Magn. Magn. Mater*. **2005**, *290 – 291*, 8 – 13.

(12) Thanh, D. T. C.; Brück, E.; Tegus, O.; Klaasse, J. C. P.; Gortenmulder, T. J.; Buschow, K. H. J. Magnetocaloric effect in MnFe(P,Si,Ge) compounds. *J. Appl. Phys*. **2006**, *99*, 08Q107-1 – 08Q107-3.

(13) Engelbrecht, K.; Nellis, G. F.; Klein, S. A. Zimm, C. B. Recent Developments in Room Temperature Active Magnetic Regenerative Refrigeration. *HVAC&R Research*. **2007**, *13*, 525.

(14) Pecharsky, V. K.; Gschneidner, K. A. Jr. Thirty years of near room temperature magnetic cooling: Where we are today and future prospects. *Int. J. Refrig.* **2008**, *31*, 945.

(15) Zimm, C.; Jastrab, A.; Sternberg, A.; Pecharsky, V. K.; Gschneidner, K. A. Jr.; Osborne, M.; Anderson, I. Description and Performance of a Near-Room Temperature Magnetic Refrigerator. *Adv. Cryog. Eng.* **1998**, *43*, 1759.

(16) He, A.; Svitlyk, V.; Mozharivskyj, Y. Synthetic Approach for $(Mn,Fe)_2(Si,P)$ Magnetocaloric Materials: Purity, Structural, Magnetic, and Magnetocaloric Properties. *Inorganic Chemistry*. **2017**, 56, 2827-2833.

(17) Hunter, B. A.; Howard, C. J. Rietica; Australian Nuclear Science and Technology Organization: Menai, Australia, **2000**.

(18) Sheldrick, G. M. *SHELXL97 and SHELXS97*, University of Gottigen: Germany, **1997**.

(19) Höglin, V.; Cedervall, J.; Andersson, M. S.; Sarkar, T.; Hudl, M.; Nordblad, P.; Andersson, Y.; Sahlberg, M. Phase diagram, structures and magnetism of the $FeMnP_{1-x}Si_x$ - system. *RSC Advances*. **2015**, *5*, 8278-8284.